

RESEARCH ARTICLE

10.1002/2016JC012348

Striations and preferred eddy tracks triggered by topographic steering of the background flow in the eastern South Pacific

Ali Belmadani^{1,2} , Emilio Concha¹ , David Donoso¹, Alexis Chaigneau³, François Colas⁴ , Nikolai Maximenko⁵ , and Emanuele Di Lorenzo⁶ 

Key Points:

- Striations coincide with polarized eddy tracks and the offshore formation of new eddies
- Vorticity produced by topographically steered unstable meridional flow triggers striations as β -plumes
- Eddy vorticity advection and striation shear instability participate to maintain eddy streets and striations

Correspondence to:

A. Belmadani,
abelmadani@dgeo.udec.cl

Citation:

Belmadani, A., E. Concha, D. Donoso, A. Chaigneau, F. Colas, N. Maximenko, and E. Di Lorenzo (2017), Striations and preferred eddy tracks triggered by topographic steering of the background flow in the eastern South Pacific, *J. Geophys. Res. Oceans*, 122, 2847–2870, doi:10.1002/2016JC012348.

Received 16 SEP 2016

Accepted 6 MAR 2017

Accepted article online 11 MAR 2017

Published online 4 APR 2017

¹Department of Geophysics, University of Concepcion, Concepcion, Chile, ²Millennium Institute of Oceanography, University of Concepcion, Concepcion, Chile, ³Laboratoire d'Études en Géophysique et Océanographie Spatiale, Université de Toulouse, CNES, CNRS, IRD, UPS, Toulouse, France, ⁴LOCEAN/IRD/IPSL/UPMC, Paris, France, ⁵International Pacific Research Center, School of Ocean and Earth Science and Technology, University of Hawaii at Manoa, Honolulu, Hawaii, USA, ⁶School of Earth and Atmospheric Sciences, Georgia Institute of Technology, Atlanta, Georgia, USA

Abstract In recent years, persistent quasi-zonal jets or striations have been ubiquitously detected in the world ocean using satellite and in situ data as well as numerical models. This study aims at determining the role of mesoscale eddies in the generation and persistence of striations off Chile in the eastern South Pacific. A 50 year climatological integration of an eddy-resolving numerical ocean model is used to assess the long-term persistence of striations. Automated eddy tracking algorithms are applied to the model outputs and altimetry data. Results reveal that striations coincide with both polarized eddy tracks and the offshore formation of new eddies in the subtropical front and coastal transition zone, without any significant decay over time that discards random eddies as a primary driver of the striations. Localized patches of vortex stretching and relative vorticity advection, alternating meridionally near the eastern edge of the subtropical front, are associated with topographic steering of the background flow in the presence of steep topography, and with baroclinically and barotropically unstable meridional flow. These sinks and sources of vorticity are suggested to generate the banded structure further west, consistently with a β -plume mechanism. On the other hand, zonal/meridional eddy advection of relative vorticity and the associated Reynolds stress covariance are consistent with eddy deformation over rough topography and participate to sustain the striations in the far field. Shear instability of mean striations is proposed to feedback onto the eddy field, acting to maintain the subtropical front eddy streets and thus the striations.

1. Introduction

In recent years, ubiquitous quasi-zonal mesoscale jet-like features have been detected in the time-mean circulation of the world ocean [Maximenko *et al.*, 2005, 2008; Richards *et al.*, 2006; Centurioni *et al.*, 2008; Cravatte *et al.*, 2012]. These alternating bands of eastward/westward flow have a meridional wavelength of 300–500 km, are vertically coherent over several hundred meters depth with a surface intensification, and extend zonally for thousands of kilometers. Although weak (~ 1 cm/s), these jets (or striations) may be able to advect the background temperature field [Buckingham *et al.*, 2014], contribute to tracer mixing [Chen and Flierl, 2015], transport surface-drifting marine debris [Maes *et al.*, 2016], and modify low-level winds [Taguchi *et al.*, 2012], with potential implications for marine ecosystems and climate.

Despite their ubiquity, little is known about these jet-like features. There is an ongoing debate on their nature and origin. Striations are usually not distinguished in snapshots of observed sea level, which is dominated by mesoscale eddies [Chelton *et al.*, 2011a] and are only seen after time-averaging over months to years [Maximenko *et al.*, 2005] or low-pass filtering in the frequency domain [Ivanov *et al.*, 2009; Chen *et al.*, 2015]. Besides, horizontal high-pass-filtering is often required to isolate striations from the usually stronger background flow [Maximenko *et al.*, 2008, hereinafter MNS08]. In addition, the quasi-zonal striations tend to cross the mostly meridional mean dynamic ocean topography (MDOT) contours in subtropical gyres, so that water particles move across striations rather than along them (MNS08). For these reasons, they are not universally accepted as real jets, and several theories have emerged to explain their existence.

1.1. Theories for the Existence of Striations

The null-hypothesis is that striations are artifacts of time-averaging westward propagating eddies [Qiu *et al.*, 2008]: zonal swirl velocities on the northern/southern flanks of an individual vortex should leave a jet-like signature in the mean velocity field, while meridional swirl velocities cancel out [Scott *et al.*, 2008]. Using an idealized model of random eddies with statistical characteristics derived from observations, Schlax and Chelton [2008, hereinafter SC08] found banded structures in 10 year averaged zonal velocity similar to striations observed off California and west of Hawaii. Their amplitude decayed inversely with the averaging period, and a small number of strong, large eddies were the main contributors to the striated pattern, suggesting that the 20 year observational record is too short for unambiguous detection of striations. On the other hand, Buckingham and Cornillon [2013, hereinafter BC13] estimated that eddies identified in the eastern South Pacific (ESP) over a 16 year period from absolute dynamic topography (MDOT plus sea level anomaly) are significant but not unique contributors to striations. These eddies have various amplitudes and sizes, and the mean zonal velocity decays more slowly compared to the inverse relation, suggesting that SC08's random eddies alone cannot explain the existence of striations [Ivanov *et al.*, 2012].

An alternate explanation is that striations are the result of organized eddies following preferred pathways [Maximenko *et al.*, 2005; Scott *et al.*, 2008]. For example, eddy tracks off California show alternating bands of dense/sparse eddy traffic (SC08), with orientation and locations consistent with striations (MNS08, Figure 2e). Besides, quasi-zonal bands of alternating preference for cyclonic/anticyclonic eddies were ubiquitously found in 22 year global altimeter records [Chelton *et al.*, 2011a; see also <http://cioss.coas.oregonstate.edu/eddies/>]. While time averaging these bands should produce striations, whether they are persistent, vary over time [Ivanov *et al.*, 2009], or arise from inadequate sampling of random eddies is unclear. One possibility is the existence of preferred eddy generation sites along eastern boundaries, such as permanent meanders of the California Current [Centurioni *et al.*, 2008, hereinafter CON08] or radiating instabilities of an eastern boundary current (EBC) [Wang *et al.*, 2012, 2013].

Indeed, combining surface drifting buoys and satellite altimetry, CON08 revealed the presence of four meanders in the California Current and four pairs of striations extending from these for several thousand kilometers. They proposed that vorticity sources/sinks associated with permanent meanders radiate Rossby waves that form stationary jets in the ocean interior, a mechanism known as β -plume [Rhines, 1994; Afanasyev *et al.*, 2012; Belmadani *et al.*, 2013; Davis *et al.*, 2014]. Similarly, instabilities radiating from an idealized EBC can form striations [Wang *et al.*, 2012, 2013] consistent with observations off California and central Chile (MNS08). In the turbulent real ocean, eddies may be the dominant mechanism for radiating instabilities and may interact nonlinearly with time-mean striations [Melnychenko *et al.*, 2010, hereinafter MSS10], either sustaining or dissipating them [Ivanov *et al.*, 2009] (if so, striations may not be reduced to SC08-type artifacts). In turn, baroclinic/barotropic instabilities associated with the sheared striations and background flow may generate new eddies along the jet axis [Yoshida *et al.*, 2010, 2011; MSS10]. Such nonlinear interaction may thus explain why striations/eddy streets remain coherent for long distances and over long periods of time [Chelton *et al.*, 2011a].

Striations produced by radiating instabilities decay with longer averaging periods, suggesting they are not stationary [Wang *et al.*, 2012]. It is however possible that irregular coastlines and bottom topography anchor filaments, eddies, meanders [Batteen, 1997], and hence the associated striations. Indeed, Davis *et al.* [2014, hereinafter DDL14] studied the sensitivity of eastern North Pacific (ENP) striations in the Regional Oceanic Modeling System (ROMS) [Shchepetkin and McWilliams, 2005] to horizontal resolution, wind speed, bottom topography, and coastline geometry. Although their properties were sensitive to all these factors, striations vanished in the time mean only in the experiment with meridional eastern boundary due to alongshore propagation of vorticity sources.

Other theories have also been suggested. The most commonly invoked involves the so-called "Rhines mechanism," where barotropic turbulence on a rotating sphere tends to self-organize into zonal jets through the merging of coherent vortices [Rhines, 1975]. Their meridional "Rhines" scale is consistent with striations in numerical models [Nakano and Hasumi, 2005; Richards *et al.*, 2006] but not in observations [Maximenko *et al.*, 2005]. Besides, MSS10 computed potential vorticity (PV) budgets of striations off California and Chile from observations and a model and found that eddy forcing was inconsistent with the Rhines mechanism. Furthermore, whereas the latter may apply to zonal jets in the atmospheres of giant planets

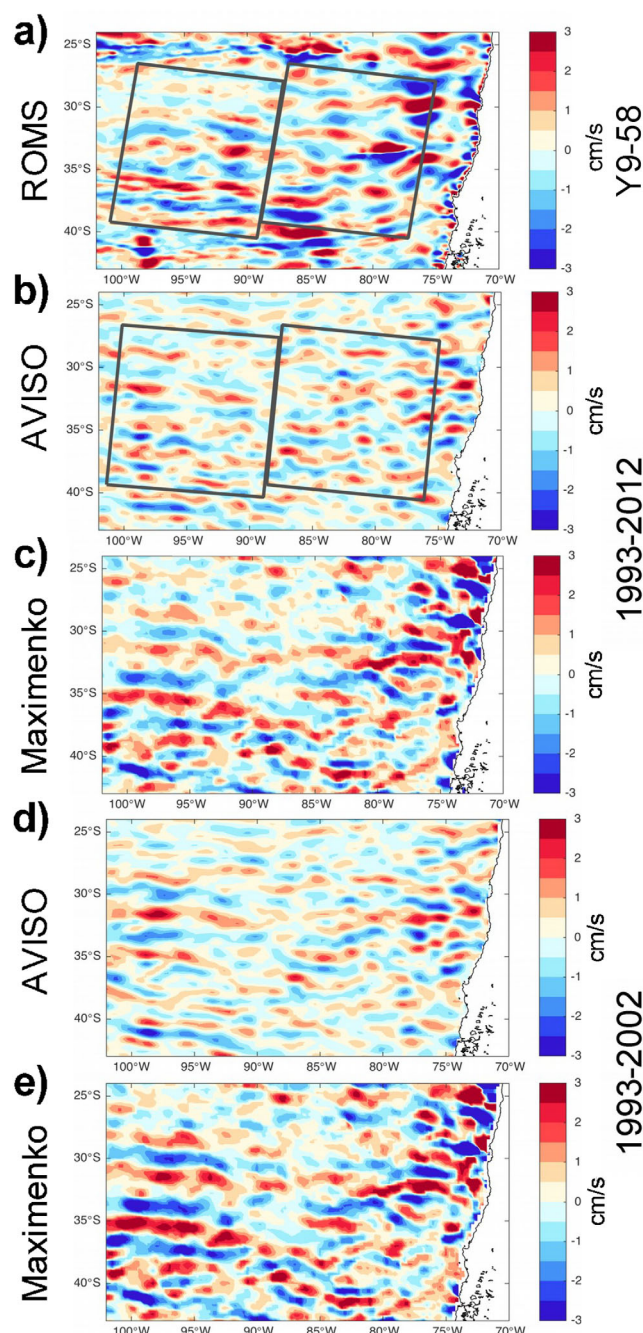


Figure 1. Mean spatially high-pass filtered surface geostrophic zonal velocity (cm s^{-1}) from (a) ROMS averaged over model years 9–58, and from (b, c) MDT averaged over 1993–2012 from (b) AVISO MDT_CNES-CLS13 and (c) *Maximenko et al.* [2014], the latter being interpolated to a 0.5° grid and smoothed with a 2-D median filter (0.5° half width). (d, e) Same as Figures 1b and 1c, except that AVISO SLA averaged over 1993–2002 was added to MDT fields. The black boxes in Figures 1a and 1b are tilted with the average striation angle in ROMS (-8°) and AVISO MDT_CNES-CLS13 (-5°), respectively, determined from 2-D Fourier analysis (see text).

(MNS08, MSS10, and BC13) (Figure 1), similar in many ways to its northern hemisphere counterpart, including the presence of an EBC, the Humboldt Current.

On the other hand, mesoscale eddies have been extensively studied in the ESP [Chaigneau and Pizarro, 2005a; Correa-Ramirez et al., 2007; Chelton et al., 2011b; Colas et al., 2012; Combes et al., 2015; Pegliasco et al.,

with mostly zonal flow [Galperin et al., 2004], it fails to explain how striations in ocean gyres cross mean PV contours (MNS08).

1.2. Focus of This Study

A key question is whether striations really are persistent (MNS08, CON08, BC13, and DDL14) or if they only appear so due to inadequate sampling over the satellite era [Chelton et al., 2011a; SC08]. Previous studies have not succeeded to address this question unequivocally as they were based on either “short” observed time series [Scott et al., 2008; Chelton et al., 2011a; MNS08; CON08; BC13] or idealized models with distant real-ocean application [Wang et al., 2013; SC08]. An exception is DDL14’s use of 120 year climatological simulations to study North Pacific striations in a semirealistic framework, but they mostly restricted their analysis to the first 10 years, leaving the significance of stationary striations in the presence of a realistic EBC subject to discussion. A main goal of the present study is to bridge the gap between observation and theory-based studies by using a long simulation similar to DDL14 and comparing it to satellite altimetry data.

Most previous works have focused on EBC regions since the mean circulation and eddy activity are relatively weak there, allowing easier detection of striations (MNS08 and MSS10), and since they are privileged locations for radiating instabilities and β -plumes [Afanasyev et al., 2012; Wang et al., 2013]. Because of the wealth of historical data and modeling efforts, the California Current and the ENP have received a lot of attention [Ivanov et al., 2012; Wang et al., 2012; Chen et al., 2015; SC08; CON08; DDL14]. Yet both observations and models indicate particularly clear striations off the coast of central Chile in the ESP

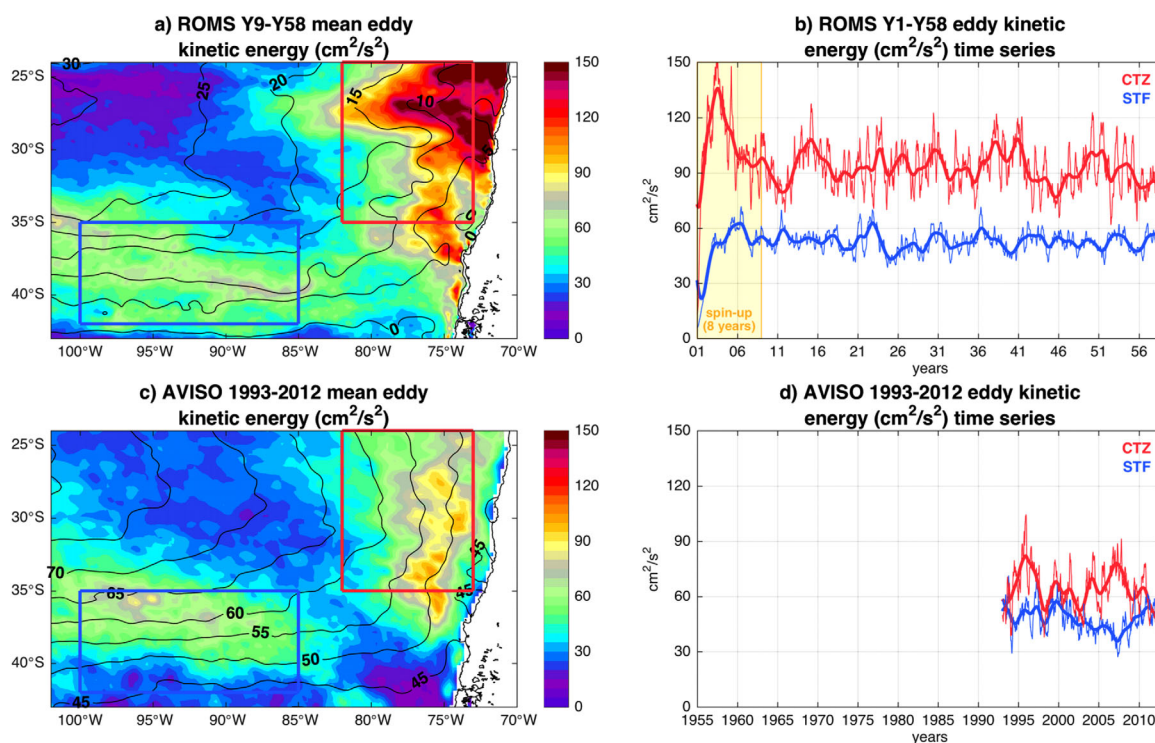


Figure 2. (a, c) Mean surface geostrophic EKE ($\text{cm}^2 \text{s}^{-2}$) in (a) ROMS averaged over model years 9–58 and (c) AVISO averaged over 1993–2012, with contours of (a) mean SSH and (c) MDOT overlaid (contour interval is 5 cm). (b, d) Time series of monthly mean EKE averaged over the CTZ (thin red lines) and STF (thin blue lines) in (b) ROMS and (d) AVISO. Low-pass filtered EKE time series with a 12 month wide moving window are also shown (thick red/blue lines). The red and blue boxes in Figures 2a and 2c indicate the locations of the CTZ and STF, respectively.

2015]. They are generated near the coast of South America [Chaigneau *et al.*, 2009] and in the coastal transition zone (CTZ) off central Chile (29°S – 39°S) where eddy kinetic energy (EKE) is locally maximum, partly from baroclinic instability of coastal currents [Hormazabal *et al.*, 2004; Capet *et al.*, 2008]. While cyclonic/anticyclonic eddies were found to diverge by propagating westward/northwestward, respectively [Chaigneau and Pizarro, 2005a], due to the β effect and PV conservation [Morrow *et al.*, 2004; Cushman-Roisin and Beckers, 2011], narrow bands of alternating eddy polarity have also been found [Chelton *et al.*, 2011a; see also Chaigneau *et al.*, 2009, Figure 2b] and suggest the existence of preferred eddy pathways in this region, too (BC13).

This study focuses on the dynamics of striations and eddies off Chile by implementing a long climatological integration of a high-resolution regional ocean model of the eastern South Pacific Ocean. The paper is organized as follows: in section 2, the model, altimetry, and MDOT data are presented, together with the methodology. The model striations and eddies are validated against observations in section 3. Stationary striations and their relationship with mean eddy tracks as well as bottom topography are analyzed in section 4. Section 5 discusses the results before concluding.

2. Data and Methods

2.1. Numerical Model

The ROMS regional ocean model solves the hydrostatic primitive equations with a free-surface explicit scheme and stretched terrain-following vertical coordinates. It has successfully reproduced striations in a subtropical gyre (DDL14), stationary meanders of an EBC (CON08), and mesoscale activity in the ESP [Colas *et al.*, 2012; Combes *et al.*, 2015]. The rectangular domain (22°S – 45°S , 105°W – 70°W) includes the eastern part of the South Pacific subtropical gyre and embedded striations (MNS08), with open boundaries at the northern, western, and southern sides. It is bordered by the coast of South America to the east and the East Pacific Rise to the west. An eddy-resolving 0.1° resolution is used (~ 9 km at 30°S – 40°S), which has been shown to capture ESP striations (MNS08; MSS10). Mesoscale eddies have typical diameters of 100–150 km

in this region [Chaigneau *et al.*, 2009], which are resolved by 10–15 grid points. 32 vertical levels refined near the surface are used. Bottom topography is from ETOPO1 [Amante and Eakins, 2009], smoothed to reduce pressure gradient errors [Beckmann and Haidvogel, 1993]. A 150 km wide sponge layer is used along the open boundaries, where horizontal viscosity/diffusivity increase linearly from 0 at the interior to $100 \text{ m}^2 \text{ s}^{-1}$ along the boundaries. There is no explicit horizontal mixing outside the sponge layer; instead, the model relies on a third-order upstream-biased advection operator.

The model was forced with the monthly 25 km Scatterometer Climatology of Ocean Winds (SCOW) [Risien and Chelton, 2008] and air/sea fluxes from the 2.5° National Centers for Environmental Prediction (NCEP)/National Center for Atmospheric Research (NCAR) Reanalysis I (hereafter NCEP) [Kalnay *et al.*, 1996]. SCOW winds were preferred to those from NCEP because the latter produces biased nearshore circulation and coastal upwelling [Colas *et al.*, 2012; Cambon *et al.*, 2013]. Heat fluxes include Newtonian restoring to Reynolds 1.875° monthly climatological SST [Smith and Reynolds, 1998] and to the Commonwealth Scientific and Industrial Research Organisation (CSIRO) Atlas of Regional Seas (CARS) 2009 0.5° monthly climatological sea surface salinity [Dunn and Ridgway, 2002].

A monthly climatology derived from the last 6 years (the only available data) of a 50 year climatological integration of the Ocean General Circulation Model for the Earth Simulator (OFES) [Masumoto *et al.*, 2004] forced by NCEP and averaged over a reduced 0.5° grid provides the initial and open boundary conditions for density, horizontal velocity, and sea level. The data were previously smoothed with a 2-D median filter (0.5° half width) to eliminate residual mesoscale structures. The choice of OFES is motivated by its ability to resolve the gyre in which realistic striations are embedded (MNS08 and MSS10). The simulation was run for 50 years after an 8 year spin-up to assess the long-term persistence of striations. Model outputs were saved every 2 days to allow accurate mesoscale eddy tracking (see below). An additional experiment identical to the former control run except with a flat bottom of depth 4000 m was performed to assess the sensitivity of the model circulation to bottom topography.

2.2. Altimetry Data and Mean Dynamic Ocean Topography

AVISO SSALTO/DUACS DT2014 satellite altimetry data are used to validate model mesoscale eddy statistics and EKE, as well as characterize the observed relation between striations and organized eddies. Daily delayed-time (DT) reference series (Ref) from January 1993 to December 2012 on a $1/4^\circ$ grid result from optimal interpolation of measurements from a maximum of two satellites at any time to ensure a stable and homogeneous 20 year record [Pujol *et al.*, 2016]. Sea level anomalies (SLA) with respect to 1993–2012 are used to compute surface geostrophic EKE, while absolute dynamic topography (ADT) is used to map the time series of observed striations and to detect/track eddies over time (see section 2.3).

MDOT is used to map the mean observed surface geostrophic flow at the large scale (subtropical gyre) and mesoscale (striations) and compare to model estimates. Unless stated otherwise, MDOT is from AVISO MDT_CNES-CLS13, a $1/4^\circ$ estimate of the mean sea surface height (SSH) above the geoid over 1993–2012 used to compute ADT from SLA [Rio *et al.*, 2013]. The 1992–2012 MDOT computed by Maximenko *et al.* [2014] from near-surface drifters is also used to assess the uncertainty in the observed striations. A major difference with MDT_CNES-CLS13 is that hydrography is not used. Thanks to nearly doubled data coverage compared to the previous 1992–2002 MDOT [Maximenko *et al.*, 2008, 2009], the 1992–2012 MDOT is available at a higher $1/4^\circ$ resolution and is directly comparable to MDT_CNES-CLS13. The reader is invited to refer to Rio *et al.* [2013] and Maximenko *et al.* [2014] for more details.

Since both products are computed for 1993–2012 (Maximenko *et al.* [2014] includes data from October–December 1992 but it should have a weak impact on the 20 year MDOT), the reference period for AVISO SLA, they can be used to estimate MDOT over any period after January 1993 by simply adding time-mean SLA over that period. This is used to estimate the long-term persistence in the observed striations.

2.3. Tracking of Coherent Vortices

New algorithms have recently been developed to automate the detection and tracking of coherent vortices (mesoscale eddies) in an objective way, and help advancing our knowledge of their structure and variability [e.g., Isern-Fontanet *et al.*, 2003; Chelton *et al.*, 2011a; Halo *et al.*, 2014; Mason *et al.*, 2014]. Here we apply the method of Pegliasco *et al.* [2015]—first developed by Chaigneau *et al.* [2008, 2009]—to sea level from ROMS and AVISO.

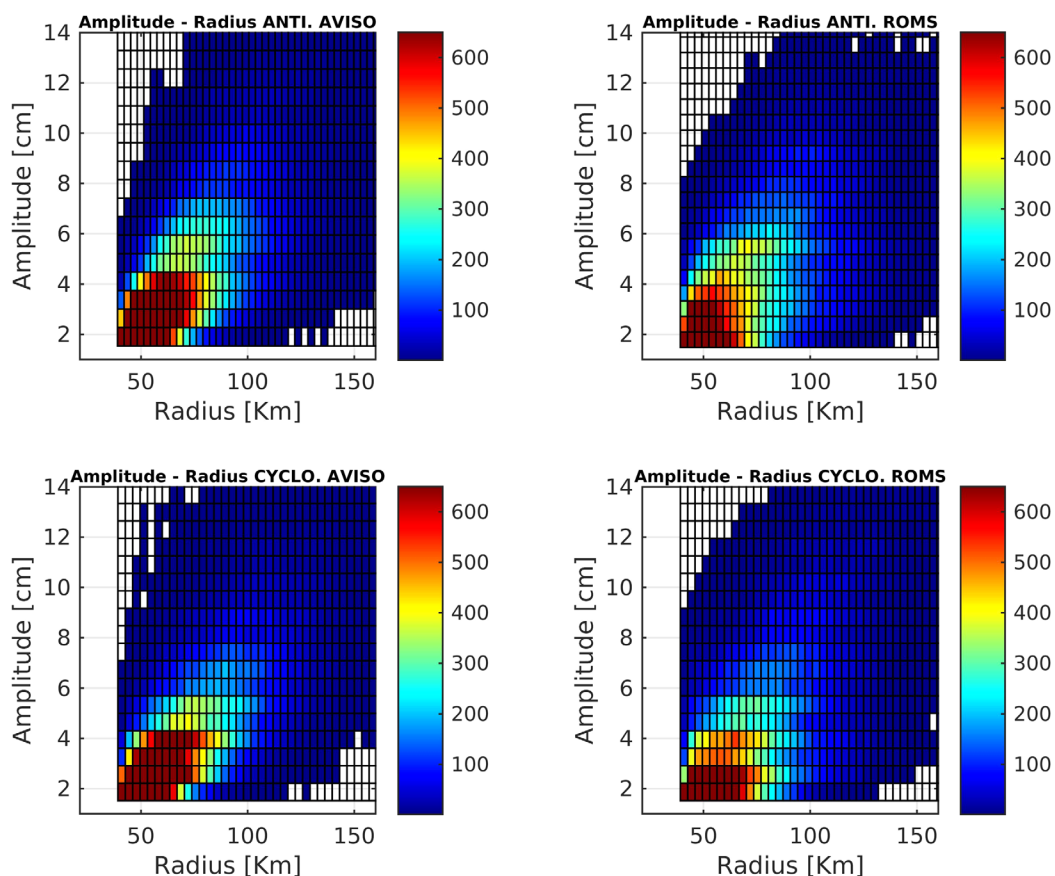


Figure 3. 2-D anticyclonic and cyclonic eddy amplitude/radius histograms in ROMS and AVISO. Only eddies with amplitude over 1 cm and duration over 30 days are considered.

As a first step (eddy detection), the algorithm detects local maxima/minima in each map of sea level, i.e., of SSH (ROMS) or ADT (AVISO), corresponding to the centers of anticyclonic/cyclonic eddies, respectively. It then searches for the outermost closed sea level contour around each eddy center that does not contain any other center, which is then defined as the eddy edge. As a second step (eddy tracking), the algorithm determines trajectories based on the vortices detected at each time step and a contour-intersection method. See *Pegliasco et al.* [2015] for more details.

Eddy trajectories are used to identify the locations of eddy generation. Eddy splits and mergers are excluded from our definition of eddy generation in order to consider only “true” new eddies. However, eddy mergers are analyzed separately to identify patterns of merging cyclonic versus anticyclonic eddies and compare them to those obtained with the same eddies before they start interacting and eventually merging. The goal is to test the relevance of the Rhines mechanism for the existence of preferred eddy pathways. The criterion for eddy interaction is that the respective centroids are distant by 100 km or less, corresponding to typical eddy diameters in the study region (section 3.1).

The method was applied to horizontally high-pass-filtered (4° half-width Hanning window) SSH/ADT data from ROMS/AVISO, respectively. Such filter was used by MNS08 and in various subsequent studies to characterize striations by removing the large-scale circulation yet preserving mesoscales $O(50\text{--}500\text{ km})$ (BC13, Figure 3), therefore allowing more straightforward comparison of striations and preferred eddy pathways in this study.

2.4. Spectral Analysis

Following MNS08, striations are diagnosed from the model mean SSH and from MDOT (section 2.2), or from the respective mean geostrophic zonal velocity, after high-pass filtering (section 2.3). It is convenient to

average various properties quasi-zonally along the striations, thus revealing their cross-jet structure. To determine the striation horizontal scales (meridional in particular) and tilt, a 2-D Fast Fourier Transform (FFT) is applied to the filtered mean geostrophic zonal velocity maps: the tilt is at right angles with the dominant wave vector, given by the straightline between the origin and the peak spectral density in the zonal/meridional wave number space (k_x, k_y). The FFT is performed upon an area ($\sim 75.6^\circ\text{W}$ – 102.6°W , 25.1°S – 42.6°S) that excludes the model sponge layer and the continental shelf, where numerical artifacts and coastal eddy generation may influence the computed spectra.

2.5. Relative Vorticity Balance

The analysis of the model relative vorticity balance may help to understand the dynamics that give rise to striations. Indeed, thanks to a nearly geostrophic balance, the crests/troughs of the striations approximately match bands of anticyclonic/cyclonic vorticity [Maximenko et al., 2005]. Thus, the terms of the balance may be interpreted as vorticity sources/sinks that act to strengthen/weaken time-mean striations, which may shed light onto the processes responsible for their generation and persistence.

We consider a simplified steady state vorticity equation on the β -plane [Gill, 1982]

$$-\beta v - \left(u \frac{\partial \xi}{\partial x} + v \frac{\partial \xi}{\partial y} \right) + f \frac{\partial w}{\partial z} + \frac{1}{\rho_0} \frac{\partial \text{curl} \tau}{\partial z} = 0, \quad (1)$$

where u, v, w (x, y, z) are the zonal, meridional, and vertical velocity components (coordinates), respectively; $\xi = \partial v / \partial x - \partial u / \partial y$ is relative vorticity, f is the Coriolis parameter, β is its meridional gradient, ρ_0 is background seawater density (1025 kg m^{-3} in ROMS), and $\text{curl} \tau$ is fluid stress curl. The four terms in equation (1) are meridional advection of planetary vorticity, horizontal advection of relative vorticity, vortex stretching, and the curl of vertical viscosity, respectively. The balance is simplified in that vertical advection of relative vorticity $-w \partial \xi / \partial z$, the relative vorticity contribution to vortex stretching $\xi \partial w / \partial z$, and the tilting term $\partial w / \partial x \cdot \partial v / \partial z - \partial w / \partial y \cdot \partial u / \partial z$ are ignored, as they were found to be weak over the model domain.

Equation (1) is integrated over the first 300 m depth, where the model striations are strongest (not shown). Considering a rigid lid, a frictionless interior, and the surface boundary condition for fluid stress, we get the vertically integrated vorticity balance

$$-\beta V - \int_{z_0}^0 \left(u \frac{\partial \xi}{\partial x} + v \frac{\partial \xi}{\partial y} \right) dz - f w(z_0) + \frac{\text{curl} \tau_0}{\rho_0} = 0, \quad (2)$$

where V is the vertical integral of v between 0 m and $z_0 = 300$ m, and τ_0 is wind stress. For presentation purposes, this balance is further averaged zonally over selected ranges (the striation source region and far field), as will become clearer in section 4.2.

The contribution of eddies to the vorticity balance and thus to striations is analyzed with a Reynolds decomposition of the (zonal/meridional) advection term

$$-\int_{z_0}^0 \left(u \frac{\partial \xi}{\partial x} + v \frac{\partial \xi}{\partial y} \right) dz = - \left(\int_{z_0}^0 \bar{u} \frac{\partial \bar{\xi}}{\partial x} dz + \int_{z_0}^0 \bar{v} \frac{\partial \bar{\xi}}{\partial y} dz + \int_{z_0}^0 u' \frac{\partial \xi'}{\partial x} dz + \int_{z_0}^0 v' \frac{\partial \xi'}{\partial y} dz \right), \quad (3)$$

where overbars (prime marks) denote time-mean averages (anomalies).

2.6. Baroclinic and Barotropic Instabilities

As stated in section 1, baroclinic and barotropic instabilities associated with the sheared striations and background flow may generate new eddies along the striations [Yoshida et al., 2010, 2011; MSS10]. Following Marchesiello et al. [2003], we characterize these instabilities by computing energy conversion terms relevant for offshore EKE generation associated with model striations, which are the barotropic conversion ($K_m K_e$) from mean kinetic energy to EKE (barotropic instability),

$$K_m K_e = -(\overline{u' u'} \frac{\partial \bar{u}}{\partial x} + \overline{u' v'} \frac{\partial \bar{u}}{\partial y} + \overline{u' w'} \frac{\partial \bar{u}}{\partial z} + \overline{v' u'} \frac{\partial \bar{v}}{\partial x} + \overline{v' v'} \frac{\partial \bar{v}}{\partial y} + \overline{v' w'} \frac{\partial \bar{v}}{\partial z}), \quad (4)$$

and the baroclinic conversion ($P_e K_e$) from eddy available potential energy to EKE (baroclinic instability),

$$P_e K_e = \frac{-g}{\rho_0} \overline{\rho' w'}, \tag{5}$$

where ρ' is density anomaly and g is the acceleration due to gravity. Both terms were computed at each model grid point, integrated over the first 300 m depth, and zonally averaged over the longitudes where the relative vorticity balance is computed (section 4.2). The individual contributions of the six terms on the right-hand side of equation (4) are examined to characterize the type of barotropic instability involved and identify its origin.

3. Validation of Model Eddies and Striations

3.1. Mesoscale Eddy Properties

A first assessment of model eddy activity is obtained by comparing EKE with that from AVISO (Figures 2a and 2c). ROMS reproduces the mean AVISO EKE reasonably well, with a maximum in the CTZ near 25°S–35°S [Hormazabal et al., 2004] and a secondary maximum in the so-called subtropical front (STF) near 35°S–40°S, 85°W–100°W [Chaigneau and Pizarro, 2005b]. The STF separates warmer and saltier subtropical water to the North from colder and fresher subantarctic water to the South, and is associated with the eastward South Pacific Current [Stramma et al., 1995; Chaigneau and Pizarro, 2005b] seen in both model outputs and MDOT data (near-zonal sea level contours in Figures 2a and 2c). The model however overestimates EKE in the CTZ by ~50% and exhibits wider EKE patches in the CTZ and STF compared to altimetry data, which may be partly due to higher resolution in ROMS and to possibly small horizontal mixing. It is not uncommon for regional ocean models to exhibit such biases in EKE in this region [e.g., Belmadani et al., 2012; Colas et al., 2012; Combes et al., 2015], but in our opinion these are modest and not critical. Note also that because of AVISO data contamination near the coast, EKE may be underestimated there compared to the model, a limitation of altimetry data common to eastern boundary systems as discussed by Capet et al. [2008].

Time series of EKE averaged over the two regions show similar levels of low-frequency modulation in the model and satellite data (Figures 2b and 2d), although they cannot be compared directly due to the climatological ROMS simulation and the significant fraction of internal eddy variability in both data sets. A Fourier analysis however reveals that ROMS and AVISO have very similar frequencies over both regions, with significant peaks at annual and interannual time scales (2–5 years, Appendix A). Note that 8 years of model spin-up, which are excluded from subsequent analyzes, roughly correspond to the EKE stabilization time scale (Figure 2b).

Properties of individual vortices inferred from the eddy detection procedure are then compared for ROMS and AVISO for a 20 year period (Figure 3). Overall, they are similar in the two data sets: mostly small (radii <70 km) and weak (amplitudes <4 cm), with amplitude growing with radius. No major difference was found between cyclonic and anticyclonic eddies, except for their total numbers: as indicated in Table 1, there are slightly more anticyclones than cyclones in both data sets (AVISO 52/48%, ROMS 54/46%). It was checked that the level of eddy nonlinearity (estimated through the computation of average velocity within each eddy contour) is similar in ROMS and AVISO, and large enough to ensure that the detected eddies are coherent vortices rather than Rossby waves: typical swirl velocities are ~10 cm/s in the STF and ~12 cm/s in the CTZ (up to 16 cm/s for ROMS, not shown). Considering typical drift velocities of ~3 cm/s in the study region [Chaigneau and Pizarro, 2005a], this yields values of 3–4 for the nonlinearity parameter (ratio of the swirl velocity to the drift velocity), indicative of highly nonlinear eddies [Chelton et al., 2011a].

Table 1. Number of Detected Eddies Over a 20 Year Period in ROMS and AVISO^a

Data	ROMS	AVISO
Cyclones	55,286 (46%)	65,829 (48%)
Anticyclones	65,283 (54%)	70,019 (52%)
Total	120,569	135,848

^aAVISO daily data were subsampled to make them comparable to ROMS 2-daily outputs. Only eddies with amplitude over 1 cm and duration over 30 days are considered.

Note that there are ~10% less eddies in ROMS over a 20 year period (Table 1), despite the higher resolution and larger EKE (Figure 2). This may be partly due to the lack of intra-seasonal and interannual frequencies in the climatological forcing, thereby removing these time scales from the forced eddy variability in the model. Also, given the higher resolution in ROMS, a larger number of small structures are represented but filtered out as we focus on eddies with amplitudes over 1 cm and duration over 30 days, which tend to be larger [Chelton et al., 2011a]. Conversely, the AVISO gridded data tends to smooth ADT fields and to

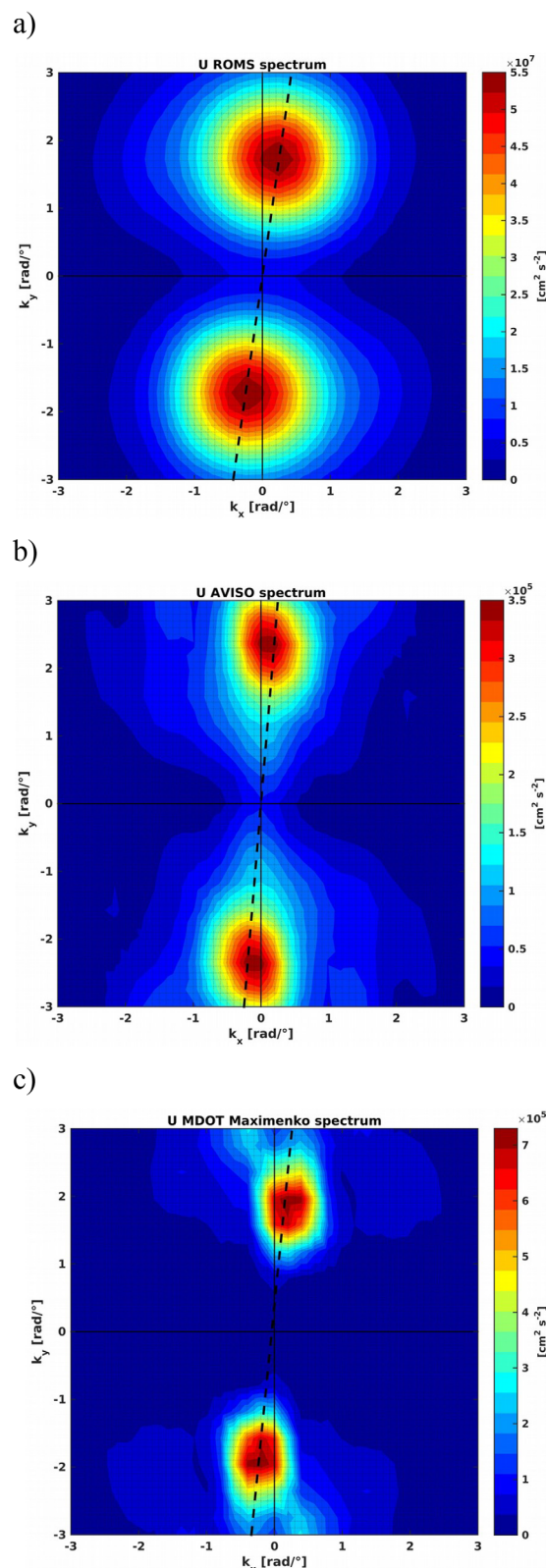


Figure 4. Spatial power spectra of mean high-pass filtered geostrophic zonal velocity ($\text{cm}^2 \text{s}^{-2}$) from (a) ROMS, (b) AVISO MDT_CNES-CLS13, and (c) *Maximenko et al.* [2014] (see Figures 1a–1c). The dashed lines indicate the direction of the dominant wave vector.

spread out small eddies, thereby increasing their size [*Chelton et al.*, 2011a].

3.2. Mean Striations

Mean model striations are most evident in the STF (Figure 1a). They do not appear directly connected to the coast, as found by previous authors based on MDOT and OFES data, conversely to striations off California (MNS08 and MSS10). They are also seen in the CTZ, although with only half the zonal extent. On average over the domain, model striations (Figures 1a and 4a) have a large zonal scale ($L_x = 25.6^\circ$), a mesoscale in the meridional axis ($L_y = 3.7^\circ$ –410 km) and are slightly tilted in the northwest-southeast direction ($\alpha = -8^\circ$), consistently with MDT_CNES-CLS13 MDOT (Figures 1b and 4b: $L_x = 32.0^\circ$, $L_y = 2.7^\circ$ –300 km, $\alpha = -5^\circ$). Although the meridional wavelength in ROMS is larger compared to MDOT, both are within the observed range as reported in previous works (e.g., MNS08). Striations tend to be stronger (2–3 cm/s) and more regular in ROMS compared to the weaker (1–2 cm/s) and noisier bands in MDOT (Figures 1a and 1b). While the climatological integration of ROMS may contribute to the mismatch by repeating the same, smooth forcing year after year, it is surprising that striations in “real” MDOT are not better defined, as in the study by MNS08 for instance. Indeed, observed striations appear to be sensitive to the chosen product: STF striations are much better defined in the 1992–2012 MDOT by *Maximenko et al.* [2014] compared to MDT_CNES-CLS13 (Figures 1b and 1c), especially west of $\sim 85^\circ\text{W}$. On average over the ESP, spatial scales ($L_x = 32.0^\circ$, $L_y = 3.2^\circ$ –360 km) and striation tilt ($\alpha = -6^\circ$) from the former MDOT (Figures 1c and 4c) also match the model estimates better.

On the other hand, compared to the older 1992–2002 MDOT (MNS08, Figure 1a), the higher-resolution and data-richer 1992–2012 product (interpolated to a 0.5° grid and smoothed to reduce noise and allow easier comparison with MNS08) features stronger striations (~ 2 versus ~ 1 cm/s) but with a similar pattern (Figure 1c). This suggests that striations are persistent, at least over a 20 year period, and may have a larger amplitude than previously thought (striations from the unsmoothed 0.25° 1992–2012 MDOT even reach amplitudes of ~ 5 cm/s, not shown).

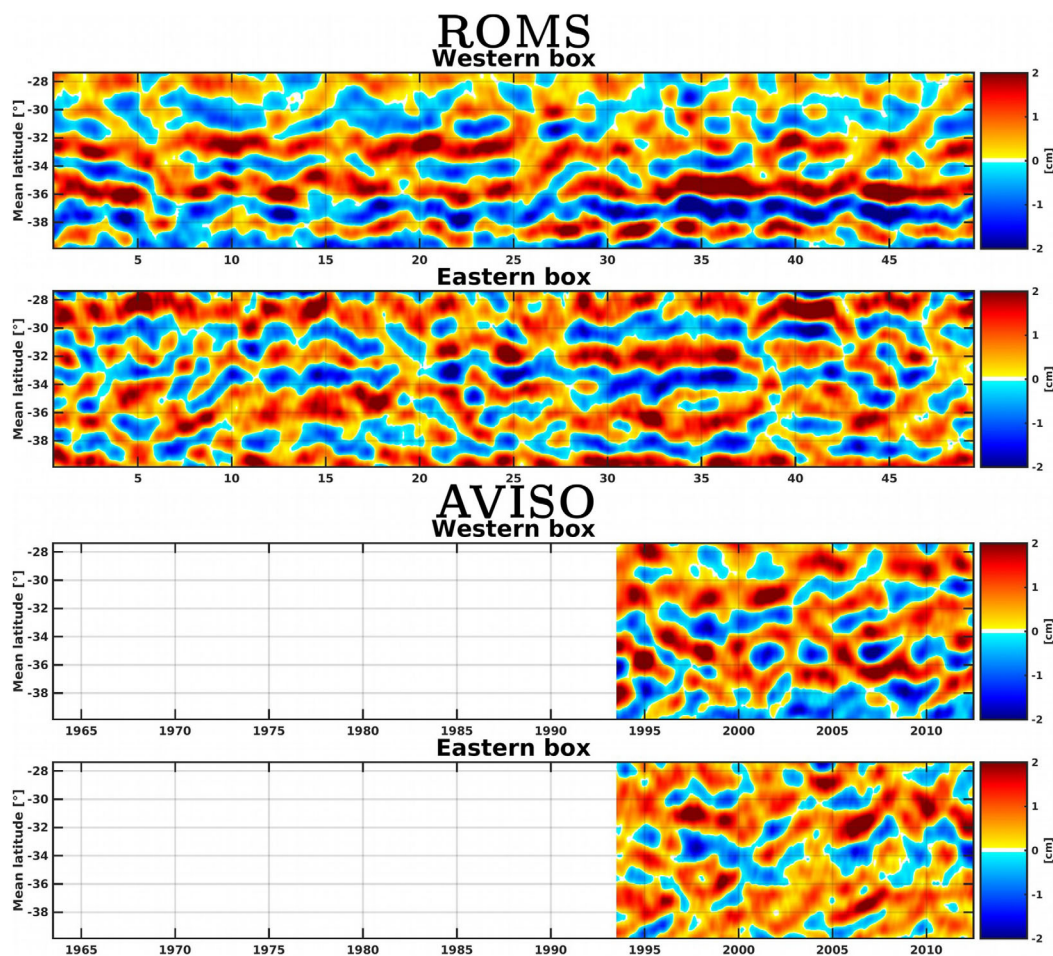


Figure 5. Time evolution of spatially high-pass filtered sea level in ROMS (SSH) and AVISO (ADT), averaged along the quasi-zonal mean striations within tilted western and eastern boxes (Figures 1a and 1b). The STF (CTZ) approximately corresponds to the 35°S–40°S (27°S–35°S) latitude range in the western (eastern) box.

SLA averaged over 1993–2002 are then added to MDT_CNES-CLS13 and *Maximenko et al.* [2014] MDT (Figures 1d and 1e), in order to assess more accurately the persistence of striations and its sensitivity to the chosen MDT, and determine whether the differences between *Maximenko et al.* [2014] and MNS08 are due to data density or to the chosen period. While MDT_CNES-CLS13 striations over 1993–2012 and 1993–2002 (Figures 1b and 1d) have similar magnitudes but different detailed structures, *Maximenko et al.* [2014] striations do not differ much whether averaged over a decade or two, except their amplitude increases to 2–3 cm/s over the shorter period (Figures 1c and 1e). This is because the time-mean SLA correlates much better with *Maximenko et al.* [2014] compared to MDT_CNES-CLS13 (not shown), suggesting the former may be more suitable to study striations in this region. From these results, it is also clear that the lower striation amplitude in the MNS08 MDT is due to data scarcity rather than long-term changes.

Overall, *Maximenko et al.* [2014] striations are as strong and well-defined as in ROMS (Figures 1a, 1c, and 1e), increasing our confidence in the model results, although the uncertainty in the observational estimates calls for caution in the interpretation of our results. It is still useful to compare striations in ROMS to those in MDT_CNES-CLS13, because averaging the latter quasi-zonally reveals smoother striations (Figure 6), and because AVISO ADT is consistent with MDT_CNES-CLS13.

4. Striations, Organized Eddies, and the Role of Topography

4.1. Stationary Striations and Preferred Eddy Tracks

To assess the long-term persistence of striations, their time evolution is examined in the model and altimetry data. In ROMS, their stationary nature is clearly seen in the STF and CTZ (Figure 5). Striations do not

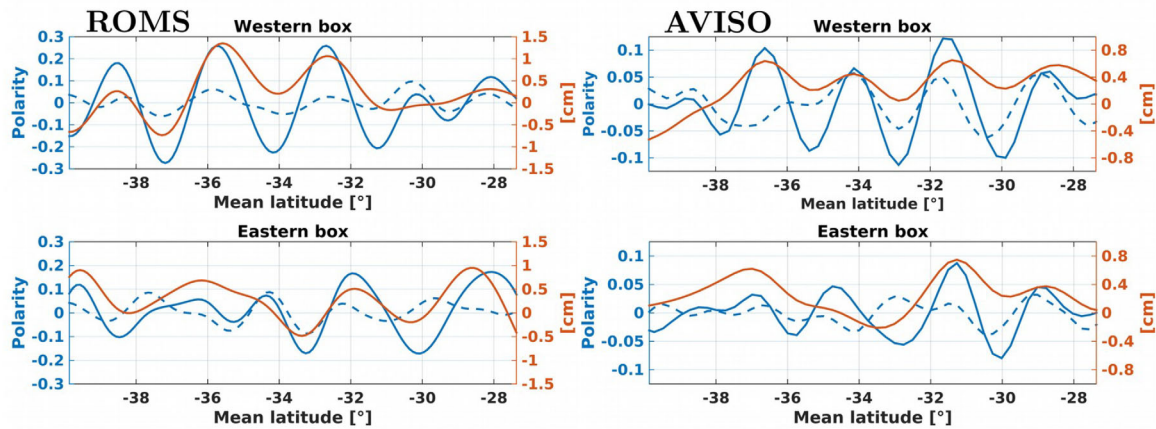


Figure 6. Mean spatially high-pass filtered sea level (solid red line), eddy polarity (solid blue line), and polarity of eddy generation (dashed blue line) in ROMS and AVISO, averaged quasi-zonally within tilted boxes (Figures 1a and 1b). The STF (CTZ) approximately corresponds to the 35°S–40°S (27°S–35°S) latitude range in the western (eastern) box. Only eddies with amplitude over 1 cm and duration over 30 days are considered for the computation of eddy polarity. Note the different y axes for ROMS and AVISO.

significantly decay over time, discarding the possibility that SC08’s random eddies cause this signal in the model. Note that it also means that time-averaging the ROMS outputs over 20 rather than 50 years would not significantly change our results, and thus that the different lengths of the ROMS and AVISO records should not be an issue for the comparison. In AVISO, the Hovmoller diagram is much noisier, as expected from the weaker and noisier mean striations in MDT_CNES-CLS13. Yet a careful examination reveals that MDT striations are also persistent but tend to phase shift in 2002–2003, possibly in response to large-scale low-frequency variability, which is absent from ROMS. This may partly explain why mean striations are not well defined in MDT_CNES-CLS13 (Figure 1b), although striations from the *Maximenko et al.* [2014] MDT are not very different over periods of a decade or two (Figures 1c and 1e). A frequency-meridional wave number 2-D Fourier analysis of the Hovmoller plots over the two regions confirms the presence of stationary striations in both ROMS and AVISO (Appendix A): on average over the record (50 and 20 years for ROMS and AVISO, respectively), stationary modes exhibit the highest energy levels, with additional energy over mesoscale modes propagating both poleward and equatorward, and generally minor differences between the two data sets.

Next, we test whether striations are the result of preferred anticyclonic/cyclonic eddy pathways by comparing the striation sea level signal to the mean polarity distribution of mesoscale eddies, defined as

$$P = \frac{N_A - N_C}{N_A + N_C}, \tag{6}$$

where N_A (N_C) is the total number of detected anticyclones (cyclones) at a given location. Thus, P represents the likelihood of anticyclones versus cyclones whenever a coherent vortex is detected at that location.

Bands of alternated eddy polarity P , indicative of polarized preferred eddy tracks, are found in the STF in both model and observed data, and to some extent in the CTZ (Figure 6, solid blue lines). These preferred tracks are clearer in ROMS, with P 2–3 times larger compared to AVISO, consistently with the stronger model striations (Figures 1a, 1b, and 6, solid red lines). Indeed, the wavy P pattern coincides with STF and CTZ striations (Figure 6): correlation coefficients are ~ 0.7 – 0.8 and 0.5 in model and observed data, respectively

Table 2. Correlation Coefficients and Maximum Lag-Correlation With Their Respective Lags Between ROMS Cross-Striation Profiles (Figure 6) of Mean SSH (MSSH) and Eddy Polarity P , MSSH and Polarity of Eddy Generation PG , P and PG^a

	Western Box			Eastern Box		
	Correlation	Max. Lag-Correlation	Lag (°)	Correlation	Max. Lag-Correlation	Lag (°)
MSSH, P	0.74	0.80	0.10	0.70	0.73	–0.20
MSSH, PG	0.26	0.27	0.10	0.20	0.30	0.40
P , PG	0.60	0.60	0.00	0.30	0.33	0.20

^aPositive (negative) lags indicate equatorward (poleward) phase shift of P in (MSSH, P) and of PG in (MSSH, PG) and (P , PG).

Table 3. Correlation Coefficients and Maximum Lag-Correlation With Their Respective Lags Between AVISO Cross-Striation Profiles (Figure 6) of MDOT and *P*, MDOT and *PG*, *P* and *PG*^a

	Western Box			Eastern Box		
	Correlation	Max. Lag-Correlation	Lag (°)	Correlation	Max. Lag-Correlation	Lag (°)
MDOT, <i>P</i>	0.51	0.51	0.00	0.52	0.52	0.00
MDOT, <i>PG</i>	0.05	0.10	0.25	0.20	0.42	0.75
<i>P</i> , <i>PG</i>	0.53	0.53	0.00	0.14	0.30	0.50

^aPositive (negative) lags indicate equatorward (poleward) phase shift of *P* in (MDOT, *P*) and of *PG* in (MDOT, *PG*) and (*P*, *PG*).

(Tables 2 and 3). These results clearly suggest that striations are the signature of polarized preferred eddy tracks.

These patterns also match bands of alternated polarity of eddy generation *PG* (the polarity of newly formed eddies, see section 2.3) to some extent, mostly in the western box (including the STF): correlation coefficients between *P* and *PG* are 0.60 and 0.53 in model and observed data, respectively, with lower values in the eastern box and between the striations and *PG* (Tables 2 and 3). These findings indicate that new eddies are formed along the STF polarized eddy tracks, suggesting a possible feedback of mean striations onto the eddy field.

On the other hand, another possibility for the existence of preferred eddy tracks is the Rhines mechanism. It is assessed by comparing *P* with the polarity of merging eddies *PM* and the polarity of these eddies before they start interacting *PB* (section 2.3): from Figure 7 it is clear that the bands in *P* do not result from eddy mergers, as they are very similar to those in *PB* and *PM*, especially for ROMS. For AVISO, although there is more discrepancy among the three patterns, *P* is not significantly more similar to *PM* than to *PB* (Figure 7 and Tables 4 and 5), which would be expected from the inverse cascade. The validity of the Rhines mechanism for the existence of preferred eddy tracks is thus not confirmed.

4.2. Origin of Striations: The Role of Bottom Topography

As stated earlier, preferred eddy pathways may result from preferred generation sites and vorticity sources/sinks in the presence of a meandering or unstable EBC. However, STF striations are only distinguished clearly west of ~85°W (Figure 1), suggesting that coastal processes may have little influence on their generation. In fact, both ROMS and AVISO clearly show that the vast majority of eddies that cross the STF are generated locally in this region, with very few eddies originating from further east (Figure 8). Note that the small nearshore patch of eddy generation at 75°W present in the model but hardly noticeable from altimetry observations is not necessarily artificial, as AVISO data are not reliable in the coastal area [Capet et al., 2008].

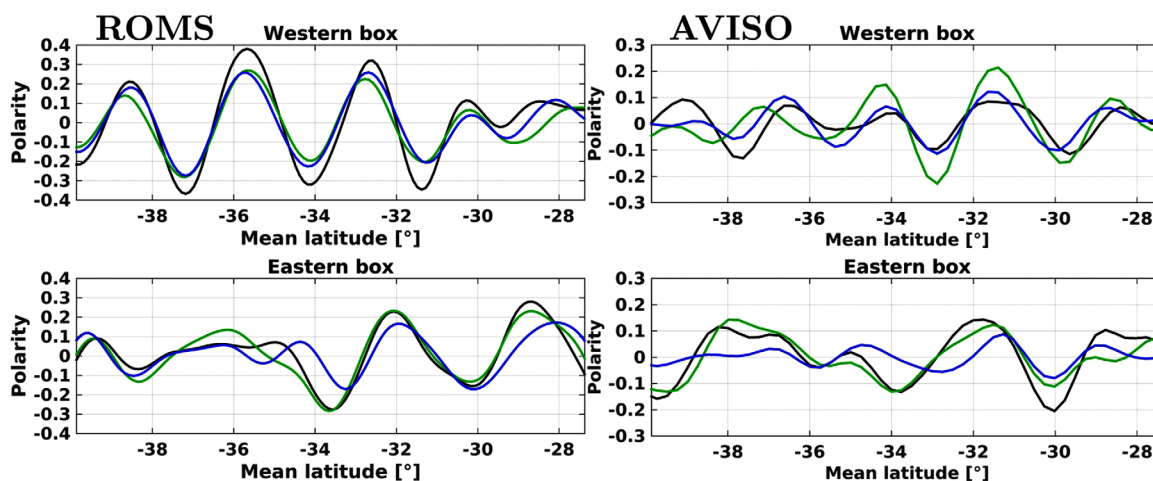


Figure 7. Same as Figure 6, except for mean spatially high-pass filtered eddy polarity (blue line, repeated from Figure 6), polarity of merging eddies (black line), and polarity of the same eddies before they start interacting (green line).

Table 4. Correlation Coefficients and Maximum Lag-Correlation With Their Respective Lags Between ROMS Cross-Striation Profiles (Figure 7) of Polarity of Merging Eddies *PM* and Polarity of These Eddies Before They Start Interacting *PB*, Mean Eddy Polarity *P* and *PB*, *P* and *PM*^a

	Western Box			Eastern Box		
	Correlation	Max. Lag-Correlation	Lag (°)	Correlation	Max. Lag-Correlation	Lag (°)
<i>PM, PB</i>	0.94	0.94	0.00	0.94	0.94	0.00
<i>P, PB</i>	0.95	0.95	0.00	0.75	0.82	0.20
<i>P, PM</i>	0.97	0.97	0.00	0.74	0.85	-0.30

^aPositive (negative) lags indicate equatorward (poleward) phase shift of *PB* in (*PM, PB*) and (*P, PB*) and of *PM* in (*P, PM*).

Table 5. Correlation Coefficients and Maximum Lag-Correlation With Their Respective Lags Between AVISO Cross-Striation Profiles (Figure 7) of *PM* and *PB*, *P* and *PB*, *P* and *PM*^a

	Western Box			Eastern Box		
	Correlation	Max. Lag-Correlation	Lag (°)	Correlation	Max. Lag-Correlation	Lag (°)
<i>PM, PB</i>	0.61	0.65	0.25	0.88	0.88	0.00
<i>P, PB</i>	0.80	0.80	0.00	0.46	0.49	0.25
<i>P, PM</i>	0.72	0.74	0.25	0.61	0.64	-0.25

^aPositive (negative) lags indicate equatorward (poleward) phase shift of *PB* in (*PM, PB*) and (*P, PB*) and of *PM* in (*P, PM*).

On the other hand, offshore bathymetry may anchor striations (BC13 and DDL14), possibly through topographically induced meandering or instability of background meridional flow. To investigate this possibility, the large-scale flow is examined by computing the mean barotropic stream function in the control run (Figure 9a). A strong eastward jet near 36°S (the South Pacific Current) spreads out east of 85°W–90°W, with broad flow veering north into the subtropical gyre and a narrow meridional jet recirculating south at 85°W, right at the eastern edge of STF striations (Figure 1a). While broad equatorward flow is expected from Sverdrup theory, the narrow poleward jet suggests a possible influence of sharp bottom topography or nonlinear processes. To separate these various contributions to the model flow, the mean barotropic stream function is computed in the flat-bottom (nonlinear) run (Figure 9b) and the Sverdrup stream function is derived from the SCOW wind stress curl (linear flat-bottom response, Figure 9c). The Sverdrup circulation is an equatorward gyre flow, with some zonal jets (Figure 9c) triggered by small-scale nearshore wind stress curl resulting from coastal orography and air-sea coupling at the oceanic mesoscale [Boé et al., 2011]. However, no zonal jet is found at 36°S and there is no recirculation, unlike in the control run. Interestingly, the flat-bottom run (with eddies) has an intermediate structure (Figure 9b): its circulation is similar to the Sverdrup flow with stronger zonal jets, an eastward jet near 37°S but weaker than in the control run and no recirculation. These results suggest that STF striations and preferred eddy tracks may result from topographic influence on the background flow, through recirculation and formation of a narrow meridional jet near

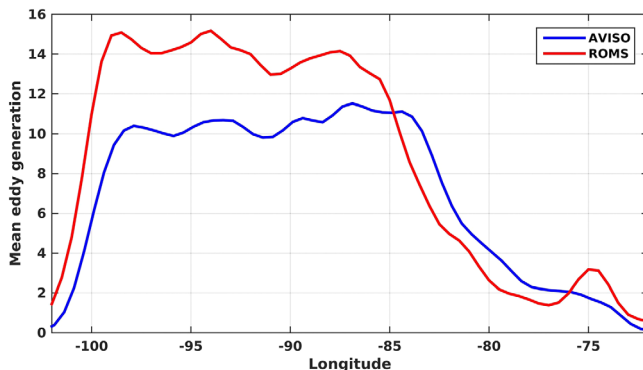


Figure 8. Number of new eddies per $0.5^\circ \times 0.5^\circ$ bin that pass through the STF (blue box in Figures 2a and 2c) at least once along their tracks, averaged meridionally from 24°S to 43°S in ROMS and AVISO. Only eddies with duration over 90 days are considered. The zonal profiles were smoothed with a 2.5° Hanning window to reduce noise.

85°W. The presence of an eastward jet in the flat-bottom run that is weaker and slightly displaced meridionally may be due at least partly to the open boundary forcing (i.e., to the presence of the South Pacific Current and STF in OFES west of 105°W). It also suggests that the STF itself may be partly controlled by bottom topography.

The influence of bottom topography is further characterized by comparing bathymetric contours with the control run barotropic stream function (Figure 10). An anticyclonic standing eddy centered at (84.5°W, 39°S) is associated with the barotropic flow meandering and recirculating southward and

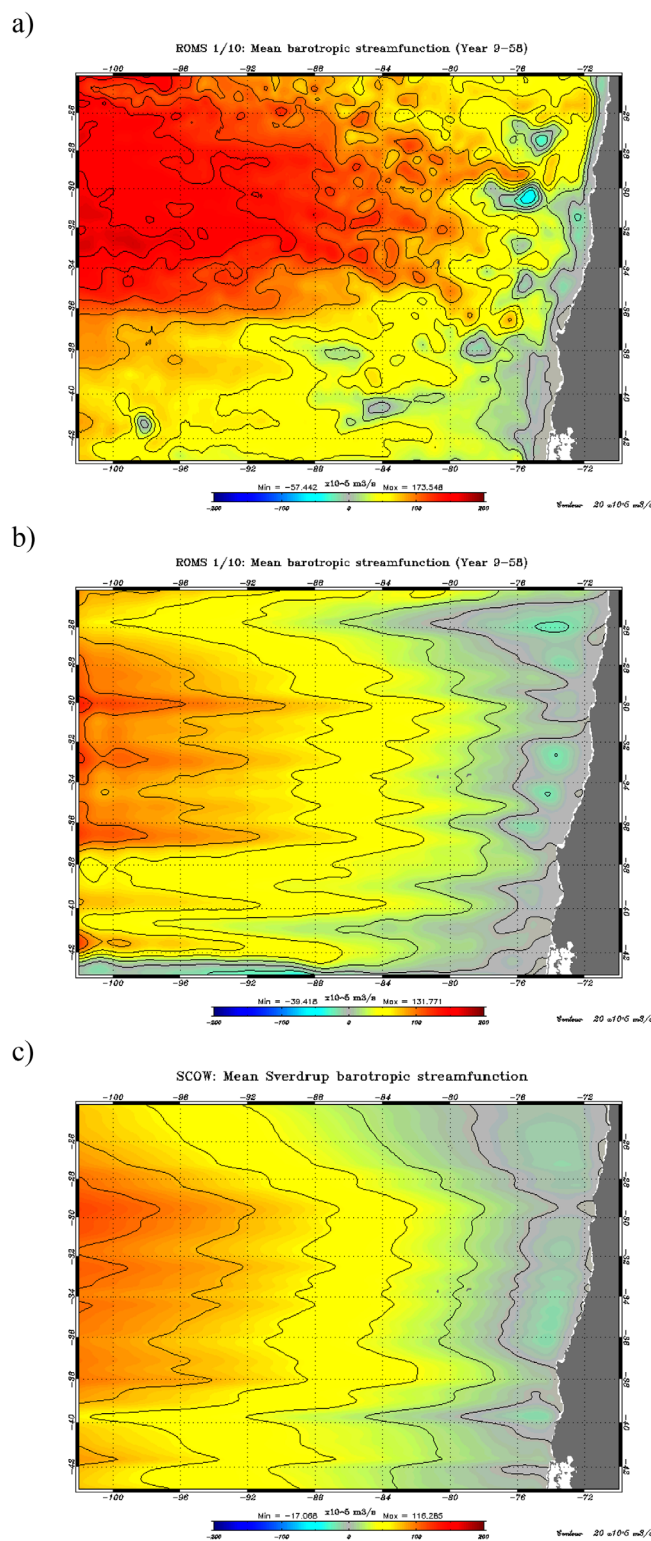


Figure 9. Mean barotropic stream function (10^{-1} Sv) in the ROMS (a) control and (b) flat-bottom runs, and (c) Sverdrup barotropic stream function (10^{-1} Sv) from SCOW. Contour interval is 2 Sv. Positive (negative) values indicate anticyclonic (cyclonic) circulation.

relatively weak residual. In particular, alternating small-scale patches of horizontal advection and vortex stretching are found near (85°W , 38°S – 42°S) in the source region, but not further west (Figure 11b). This

then eastward along sharp meridional and zonal escarpments, respectively (the associated slopes are ~ 5 m/km, see Figure 15). This is consistent with topographic steering of the South Pacific Current through PV conservation. As water particles are transported eastward, they experience a sudden increase in ocean depth, which is compensated by poleward displacement, before sharp shrinking of the water column associated with the zonal escarpment near 40°S results in flow alignment with topography. The associated standing eddy is aligned with a pair of striations of positive vorticity about 5° further west. This suggests that the likely unstable meridional jet and anticyclonic vorticity input at 85°W trigger striations via the radiation of Rossby waves and/or mesoscale eddies through a mechanism of β -plume (DDL14). About 3° further south, another eastward jet meets the top of the East Pacific Rise near (82°W , 43°S), veers northward and then eastward, with another pair of striations further west (Figure 10), suggesting similar processes are at play to generate the whole series of STF striations.

4.3. β -Plume Dynamics: Source Region Versus Far Field

A simplified relative vorticity balance is performed to identify vorticity sources/sinks that act to generate and/or maintain STF striations (section 2.5). The balance is computed in the region of flow recirculation (the source region, 83°W – 87°W / 36°S – 42°S) and further west where STF striations are found (the far field, 88°W – 96°W / 36°S – 42°S), allowing us to objectively test the β -plume hypothesis. The vorticity budget near the eastern edge of STF striations (Figure 11a) indicates that at the mesoscale (large scale), the balance is essentially between relative vorticity horizontal advection and vortex stretching (planetary vorticity meridional advection and wind stress curl, i.e., a Sverdrup balance), with a

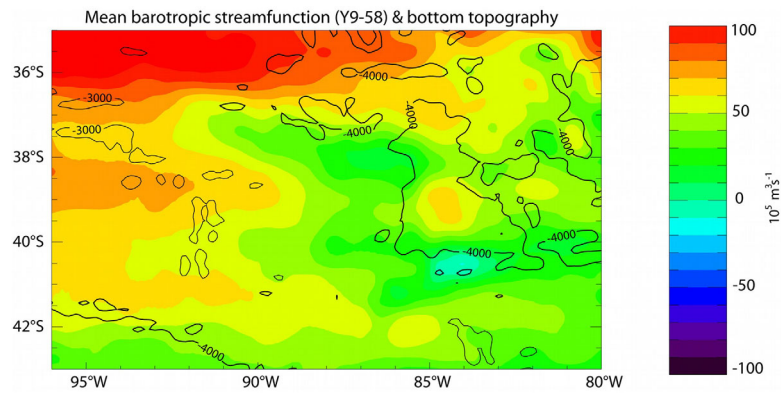


Figure 10. Mean barotropic stream function (10^{-1} Sv) in the ROMS control run, zoomed over 80°W – 96°W , 35°S – 43°S with bathymetric contours overlaid (contour interval is 1000 m). Positive (negative) values of the stream function indicate anticyclonic (cyclonic) circulation.

result supports the β -plume hypothesis, where striations develop to the west of compact patches of forcing aligned meridionally (DDL14). No term is however in phase with relative vorticity in either region (Figures 11a and 11b), failing to explain the striation wavelength and spatial phase. Note that planetary vorticity advection is equatorward over the first 300 m with a local maximum near 85°W , 39°S (Figure 11a), right where the barotropic flow recirculates poleward (Figure 9a), indicating a vertically sheared water column and suggesting the possibility of baroclinic instability (see section 4.4).

In an attempt to explain the meridional structure of relative vorticity, and given the correspondence between striations and preferred eddy tracks, the contribution of eddies to the vorticity balance is analyzed by separating horizontal advection into mean and eddy parts and further into zonal and meridional components (section 2.5). Interestingly, eddy zonal and meridional advectations ($-u'\partial\xi'/\partial x$ and $-v'\partial\xi'/\partial y$) feature banded structures both near 85°W and further west, and balance each other (Figures 12a and 12b). In particular, $-u'\partial\xi'/\partial x$ (green line) is out of phase with mean relative vorticity in both regions (black line) and is also similar to Reynolds stress cross-covariance $\overline{u'v'}$ in the STF (Figure 12b, red line), with a correlation coefficient of 0.60. On the other hand, vorticity advection by the mean currents is weak without any significant relation with relative vorticity or striated structures (Figure 12).

Such pattern is consistent with the distortion by rough bottom topography of mesoscale eddies [Ducret and Le Traon, 2001; Greatbatch et al., 2010], propagating along polarized tracks. Indeed, the ocean depth typically varies by 20–30% over 100–150 km (Figure 15), corresponding to typical eddy diameters (Figure 3), versus

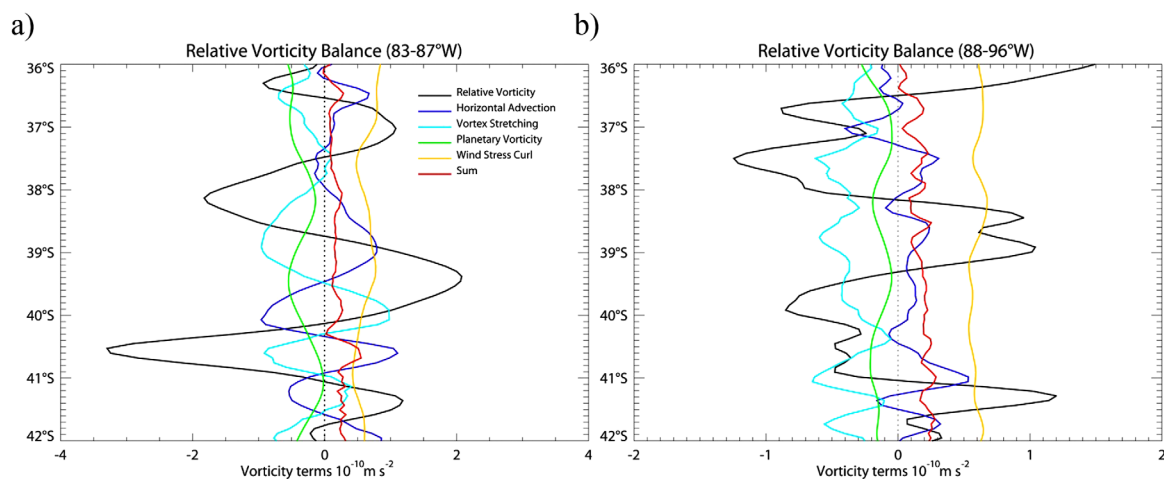


Figure 11. Simplified vertically integrated (0–300 m) steady state relative vorticity budget in the control run, zonally averaged (a) near the eastern edge of the STF (83°W – 87°W) and (b) in the STF (88°W – 96°W): horizontal advection of relative vorticity (dark blue line), vortex stretching (light blue line), meridional advection of planetary vorticity (green line), wind stress curl (yellow line), and residual (red line). Units are $10^{-10} \text{ m}^{-2} \text{ s}^{-2}$. Time-mean zonally averaged and vertically integrated relative vorticity ($10^{-4} \text{ m} \text{ s}^{-1}$, black line) is also indicated.

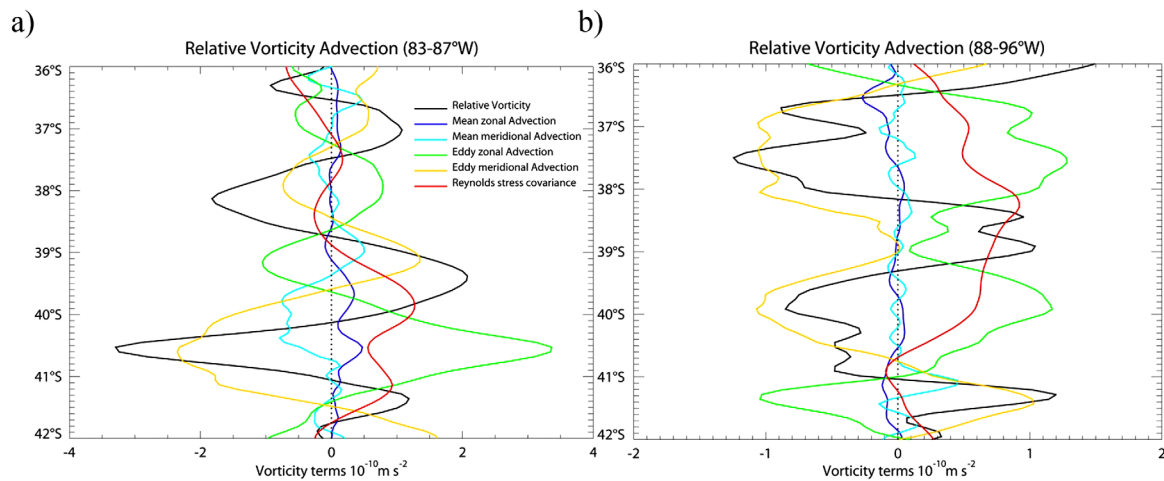


Figure 12. Decomposition of horizontal advection of relative vorticity (dark blue line in Figure 11) into mean and eddy zonal and meridional components (a) near the eastern edge of the STF (83°W–87°W) and (b) in the STF (88°W–96°W). Units are $10^{-10} \text{ m s}^{-2}$. Time-mean zonally averaged and vertically integrated relative vorticity (10^{-4} m s^{-1} , black line) and Reynolds stress cross-covariance ($10^{-1} \text{ m}^3 \text{ s}^{-2}$, red line) are also indicated.

2–3% for f (topographic β effect). In addition, meridional topography gradients dominate the ocean floor roughness with a series of zonally oriented fracture zones within the East Pacific Rise. Following similar arguments to those used by *Cushman-Roisin and Beckers* [2011, Figures 18.13 and 18.15] to explain westward and meridional drifts of mesoscale eddies, by PV conservation at the eddy scale, meridional changes in ocean depth felt by water particles must be compensated by changes in relative vorticity that may induce anisotropic swirl velocities (Figure 13). Cyclonic eddies may then be distorted northwestward or southeastward, strengthening positive (negative) $-u'\partial\xi'/\partial x$ and $\bar{u}'v'$ ($-v'\partial\xi'/\partial y$) in the respective quadrants (Figures 13a and 13c). As cyclonic eddies propagate westward along preferred tracks (band of mean negative relative vorticity), they should experience both poleward and equatorward mesoscale topography gradients (Figures 13a and 13c), resulting in a band of positive (negative) $-u'\partial\xi'/\partial x$ and $\bar{u}'v'$ ($-v'\partial\xi'/\partial y$). Similarly, anticyclonic eddies are expected to be distorted in a dominant northeast-southwest direction, resulting in overall negative (positive) $-u'\partial\xi'/\partial x$ and $\bar{u}'v'$ ($-v'\partial\xi'/\partial y$) along their paths (Figures 13b and 13d). This is a possible explanation for the out-of-phase relationship between the bands in relative vorticity or $-v'\partial\xi'/\partial y$ and those in $-u'\partial\xi'/\partial x$ or $\bar{u}'v'$ (Figure 12b).

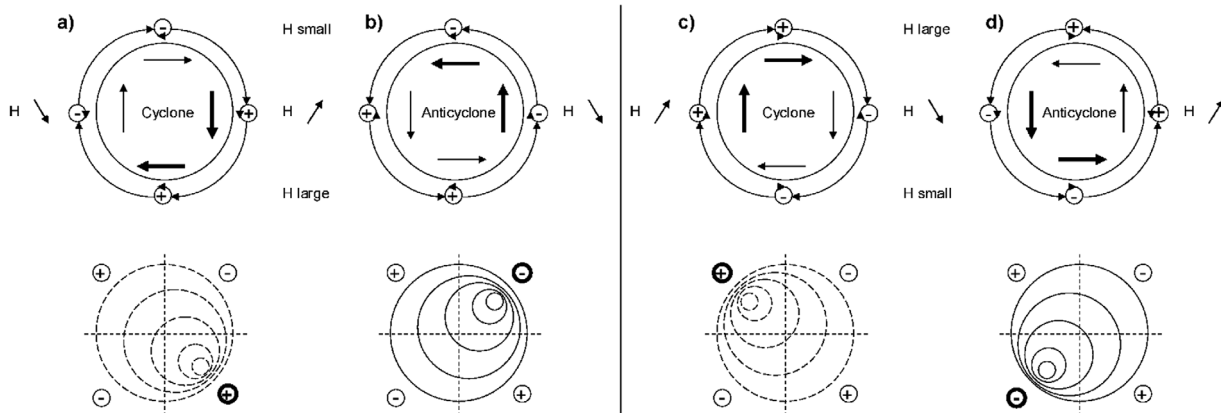


Figure 13. Sketch for eddy deformation over rough zonally oriented topography in the southern hemisphere: (a, c) cyclonic and (b, d) anticyclonic eddy embedded in mesoscale (a, b) poleward and (c, d) equatorward bathymetry gradient. (top) Meridional particle displacement along the western and eastern flanks of the eddy and associated change in ocean depth induce cyclonic (–) and anticyclonic (+) vorticities that either accelerate (thick arrows) or slow down (thin arrows) the eddy swirl. (bottom) As a result, the eddy center (vorticity extremum) is displaced toward the quadrant of maximum swirl velocity, where both Reynolds stress cross-covariance $\bar{u}'v'$ and zonal eddy advection of relative vorticity $-u'\partial\xi'/\partial x$, which have the same sign – positive (negative) in the northwestern and southeastern (northeastern and southwestern) quadrants, whatever the eddy polarity – are intensified (thick + and – signs).

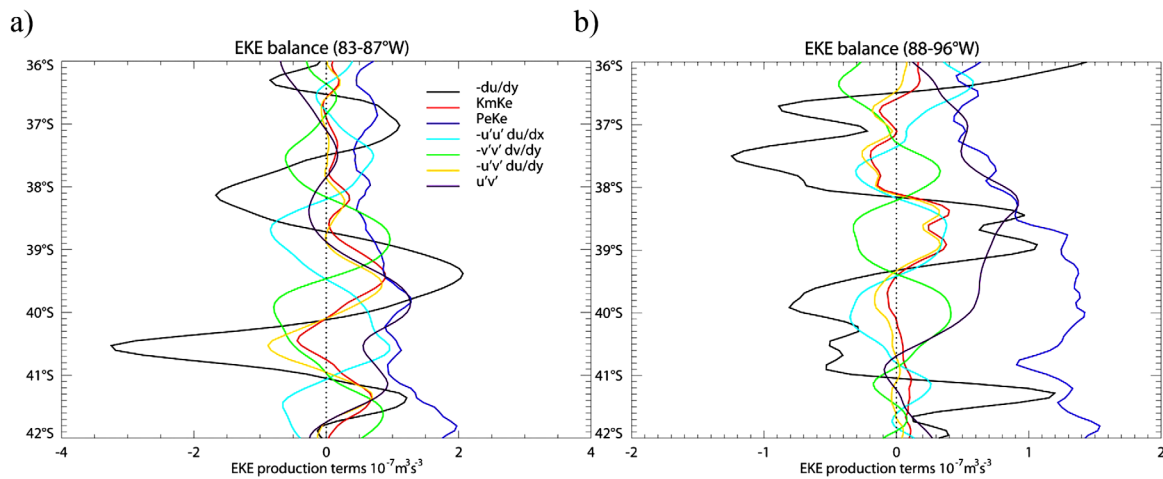


Figure 14. Vertically integrated (0–300 m) source terms for EKE in the control run, zonally averaged (a) near the eastern edge of the STF (83°W–87°W) and (b) in the STF (88°W–96°W): mean to eddy kinetic energy $K_m K_e$ (red line) and eddy available potential to kinetic energy $P_e K_e$ (dark blue line) transfers ($10^{-7} \text{ m}^3 \text{ s}^{-3}$). In addition, a simplified decomposition of $K_m K_e$ into EKE production rates from the zonal shear of the mean zonal flow $-\overline{u'v'} \partial \bar{u} / \partial x$ (light blue line) and from the meridional shear of the mean zonal $-\overline{u'v'} \partial \bar{u} / \partial y$ (yellow line) and meridional $-\overline{v'v'} \partial \bar{v} / \partial y$ (green line) flow are shown. Reynolds stress cross-covariance $\overline{u'v'}$ ($10^{-1} \text{ m}^3 \text{ s}^{-2}$, purple line) and meridional shear of the mean zonal flow times $-1 - \partial \bar{u} / \partial y$ (10^{-4} m s^{-1} , black line) are also indicated.

Eddy vorticity fluxes associated with distortion over rough topography may thus act to maintain the bands in mean relative vorticity (striations). Accordingly, purely Gaussian, nondistorted, isotropic eddies would be associated with zero zonal/meridional eddy advection and $\overline{u'v'}$, as the equally positive and negative values in each quadrant would cancel out over the quasi-zonal eddy paths. Similar behavior is expected for isotropic or random ocean floor roughness. In such cases, bands in mean vorticity may only be maintained from the source region with the β effect (i.e., artifacts of propagating eddies with preferred generation sites), rather eddy fluxes in the far field. In addition, nonzero $\overline{u'v'}$ is critical for the development of barotropic instabilities of mean striations that may act to generate new eddies as shown below.

4.4. Shear Instability of Striations: A Possible Feedback Process

A simplified EKE budget is performed to assess the potential role of baroclinic/barotropic instabilities in the generation of new eddies along the striations and at their eastern tips (section 2.6). It shows that baroclinic instability ($P_e K_e$) is positive, acting to shed eddies at the eastern edge of STF striations and further west, but without any clear relationship with mean relative vorticity (Figure 14), which is dominated by $-\partial \bar{u} / \partial y$ (compare Figures 12 and 14). On the other hand, barotropic instability ($K_m K_e$) has a banded structure in both regions that tends to be in phase with mean relative vorticity, indicating unambiguous eddy-mean interaction at the scale of striations (Figure 14), which may explain the polarized bands in eddy generation (Figure 6). The various contributors to $K_m K_e$ (equation (4)) are then examined. EKE production rates from the

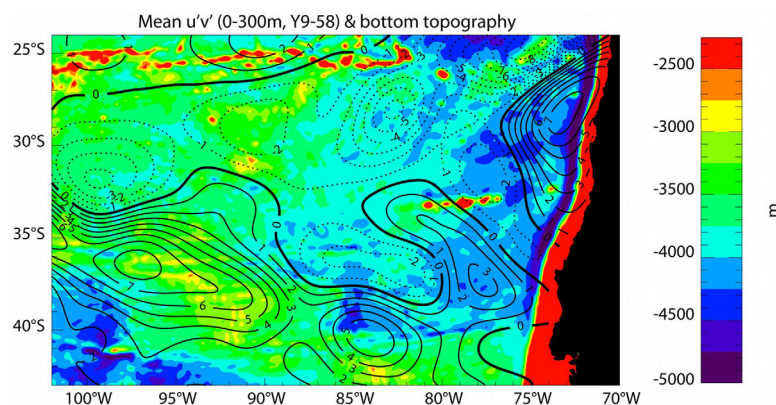


Figure 15. Bottom topography (m, shading), with contours of vertically integrated (0–300 m), spatially low-pass filtered (with a 4° half-width Hanning window) mean Reynolds stress cross-covariance $\overline{u'v'}$ overlaid (contour interval is $10^{-2} \text{ m}^3 \text{ s}^{-2}$).

zonally-sheared zonal ($-\overline{u'u'}\partial\overline{u}/\partial x$) and meridionally sheared meridional ($-\overline{v'v'}\partial\overline{v}/\partial y$) flows are large and show in-phase/out-of-phase relationships with relative vorticity in the STF (Figure 14b), respectively, but they tend to cancel out and thus do not contribute to $K_m K_e$ (Figures 14a and 14b). In contrast, EKE production from the meridionally sheared zonal flow ($-\overline{u'v'}\partial\overline{u}/\partial y$) is significant in the source region and far field, and clearly responsible for the bands in $K_m K_e$. This suggests that meridional shear instability of mean striations may feedback onto the eddy field, generating new eddies aligned with the striations. EKE production from the zonally sheared meridional flow ($-\overline{v'u'}\partial\overline{v}/\partial x$) and vertically sheared zonal/meridional flows ($-\overline{u'w'}\partial\overline{u}/\partial z$ and $-\overline{v'w'}\partial\overline{v}/\partial z$) are small over the two regions (not shown).

As stated before, $\overline{u'v'}$ correlates significantly with the banded $-\overline{u'\partial\xi'/\partial x}$ (Figure 12b), possibly due to eddy deformation over rough topography. However, a major difference is that $\overline{u'v'}$ also has a large-scale pattern and is mostly positive, allowing the banded structure in $-\overline{u'v'}\partial\overline{u}/\partial y$ and ultimately, $K_m K_e$ (Figures 14a and 14b). The large-scale structure of $\overline{u'v'}$ is likely constrained by bottom topography, as indicated by a general correspondence of positive (negative) values with shallow ridges (deep basins), at least away from the continental shelf (Figure 15), in agreement with previous studies [Ducet and Le Traon, 2001; Greatbatch et al., 2010]. This large-scale pattern may also be partly influenced by the gyre circulation, with eddies fluxing momentum into the mean zonal flow: according to the zonal momentum equation, negative (positive) meridional $\overline{u'v'}$ gradients contribute to accelerate mean eastward (westward) flow [Greatbatch et al., 2010]. Thus, the subtropical gyre (Figures 2 and 9) is consistent with meridional $\overline{u'v'}$ gradients directed away from the gyre center, which is seen in the model to some extent (Figure 15).

5. Discussion and Summary

5.1. Discussion

A major finding of this study is that STF striations appear to be generated by offshore processes, without any obvious connection to coastal dynamics. This is in striking contrast with the study by DDL14, where the model striations off California initially developed from the coast and propagated westward as mesoscale eddies to establish the mean striations, consistently with β -plume dynamics [Afanasyev et al., 2012; Belmadani et al., 2013] anchored by coastline features [Batteen, 1997]. Nevertheless, a number of similarities between the two studies may be emphasized. The generation of STF striations is also consistent with β -plumes anchored by topography (DDL14 actually found that prominent offshore topographic features could anchor some ENP striations). It also involves instabilities of a narrow meridional jet and the westward drift of mesoscale eddies. Therefore, a question that still remains is why STF striations do not also develop from the coast, as in the ENP.

Interestingly, striations attached to the coast are found in the CTZ off central-northern Chile, where the continental shelf is narrow as for most of the California coast. In contrast, the coast of central-southern Chile south of $\sim 35^\circ\text{S}$ and due east from the STF is characterized by a wider shelf. According to DDL14, the presence of a continental shelf should actually lead to stronger striations, their magnitude being constrained at the shelf by PV trapping. This is however not conclusive as the authors did not investigate these dynamics in detail. Central-southern Chile is also characterized by downwelling-favorable winds and poleward boundary currents [Strub et al., 1998], unlike the coasts of central-northern Chile or California, but similarly to northwestern United States where the coastal connection of striations is not always clear (DDL14, Figures 2a–2c). Although such correspondence may be coincidental, it seems plausible that different flow regimes induce different responses in terms of meanders, instabilities, vorticity sources, and ultimately, offshore striations.

As emphasized in section 3.2, striations from MDOT are much more sensitive to the chosen product than to the time period used to reconstruct mean sea level, which is a limitation of the study. As mentioned in section 2.2, the main difference between the Maximenko et al. [2014] and MDT_CNES-CLS13 products is that Argo dynamic height and other hydrographic profiles are not used by the former, which mostly rely for mesoscales on drifters that clearly indicate the presence of STF striations (MNS08, Figure 1b). Hydrographic and Argo data have been able to capture the striation signal [van Sebille et al., 2011; MNS08] and the vertical structure of mesoscale eddies [Chaigneau et al., 2011]. They are however subject to several limitations including scarce data coverage, especially in remote and little-studied areas such as the STF (this also applies to drifters), or Argo float trapping by subsurface-intensified eddies that contribute little to surface

signals [Colas *et al.*, 2012; Pegliasco *et al.*, 2015]. Maximenko *et al.* [2009] showed that striations can be identified on the global scale with both kinds of MDOT products. However, our results suggest that on a regional scale, they may have variable levels of skill in capturing the striated pattern. These discrepancies and the associated uncertainty raise the question of ADT data reliability for the study of mesoscale variability, striations in particular (BC13). It might be useful to reconstruct ADT from SLA and one or more MDOT products to check the robustness of results inferred from AVISO ADT.

Likewise, another limitation is the uncertainty in observational estimates of mesoscale eddies. The objective interpolation used to generate gridded altimetry data [Le Traon *et al.*, 1998] tends to introduce artifacts that resemble mesoscale eddies, which is an intrinsic limitation of automated eddy tracking in maps of the remotely sensed ocean topography [Chelton *et al.*, 2011a]. Combined with the relatively low resolution of the AVISO data, it means that preferred eddy tracks might be partly biased by these spurious features, although the clear presence of these pathways in the model gives us confidence that they are real features. The future wide-swath Surface Water and Ocean Topography (SWOT) mission, to be launched in 2019–2020 and expected to map the ocean surface at an unprecedented resolution, should help reducing significantly these uncertainties [Fu and Ferrari, 2008].

Apart from the error in the data itself, the eddy properties presented here are also subject to the uncertainty in the eddy detection and tracking algorithm of Pegliasco *et al.* [2015]. Although this uncertainty might have an impact on our results, there is some evidence that polarized preferred eddy pathways may be captured with other automated methods. As mentioned in the introduction, bands of alternating eddy polarity were found at the global scale by Chelton *et al.* [2011a], while preferred eddy tracks are clearly seen off California in the data presented by SC08. Because the map of eddy polarity presented by Chelton *et al.* [2011a, Figure 8] is noisy in our region, we downloaded their tracking results applied to weekly AVISO data and checked that bands of alternating sign indeed appear in the STF and CTZ (not shown). Yet we also applied the algorithm of Mason *et al.* [2014] to ROMS and AVISO and did not detect these bands (not shown). Although we believe that our results are robust, future studies should consider assessing the uncertainty in mesoscale patterns derived from eddy detection/tracking by intercomparing extraction methods.

Finally, an intrinsic limitation of the study is the use of a climatological simulation. Although a necessary approach to assess the long-term persistence of striations, it ignores the deterministic fraction of eddy variability at both intraseasonal and interannual-to-decadal time scales. As mentioned in section 3.2, low and high-frequency variability may impact the generation of striations and eddies, resulting in more variable, weaker or less coherent striations (as in AVISO MDOT). For example, 50–80 day coastal trapped waves triggered by equatorial Kelvin waves can propagate all the way down to central Chile [Belmadani *et al.*, 2012, and references therein]. These intraseasonal waves may be a real-ocean manifestation of the theoretical trapped modes proposed to energize nonlinear radiating instabilities and generate striations [Wang *et al.*, 2012, 2013]. On the other hand, recent work has shown that a large fraction of low-frequency eddy variability in the California Current poleward of 33°N is forced by local winds [Davis and Di Lorenzo, 2015]. Given the similarities that this region shares with the ocean off central Chile, such deterministic eddy variability may also apply to the ESP. Indeed, at the interannual scale, an enhanced eddy activity off Peru during the 1997–1998 El Niño and a reduction off central-northern Chile have been reported [Chaigneau *et al.*, 2008; Hormazabal *et al.*, 2004]. Whether these results only apply to extreme events such as the 1997–1998 El Niño is unclear, but they provide a hint that large-scale interannual variability may impact preferred eddy tracks and striations in the region. To address the high and low-frequency forcing of striations, long interannual simulations will be needed. To overcome the poor representation of EKE and coastal currents with NCEP forcing [Colas *et al.*, 2012], regional models need to be forced with high-resolution winds that could be obtained, for example, from the statistical downscaling of coarse reanalysis data [Cambon *et al.*, 2013].

5.2. Summary

A long climatological regional ocean model simulation was used together with observed mean dynamic ocean topography and altimetry data to assess the role of mesoscale eddies in the generation and persistence of striations in the eastern South Pacific off Chile. We found that striations coincide with both polarized preferred eddy tracks and the offshore formation of new eddies, without much decay over time, discarding the possibility of artifacts arising from averaging random eddies over an insufficient observational record. The inverse energy cascade hypothesis is not confirmed either, as eddy alignments are not

significantly different before and after eddies interact and merge into new eddies. Localized vorticity sources/sinks near the eastern edge of the subtropical front are associated with topographic steering of the background flow and with the resulting baroclinically and barotropically unstable meridional flow. These sources and sinks are suggested to generate the banded structure further west, consistently with β -plume dynamics. Nonlinear zonal/meridional eddy advection of relative vorticity and the associated Reynolds stress covariance are consistent with eddy deformation over anisotropic rough topography resulting from zonally oriented fracture zones within the East Pacific Rise, and participate to sustain striations in the far field. Meridional shear instability of the mean striations is proposed to feedback onto the eddy field, acting to maintain the subtropical front eddy streets and striations.

Appendix A: Comparison of Spatiotemporal Scales of Model and Observed Eddy Activity and Striations

To assess and compare the low-frequency modulation of model and observed eddy activity in the CTZ and STF, FFT of the area-averaged raw EKE time series for ROMS and AVISO (thin lines in Figures 2b and 2d) were performed in the following fashion. For each time series, we first performed FFT over the first 5 years (after applying a Hanning filter of 5 year width) and normalized the spectrum by its integral value over the frequency domain (so that the sum of all values is 1). We then repeated this step over another 5 year window that has 50% overlap with the previous one (i.e., from $t = 2.5$ years to $t = 7.5$ years), and so on to cover the whole record. We thus got 7 spectra for AVISO and 19 spectra for ROMS. We ensemble-averaged these spectra to get smooth, normalized spectra for each data set. We assessed the significance of the energy peaks against red noise by computing the normalized red noise spectra for each 5 year window and ensemble-averaging them as was done for the EKE spectra. The individual red noise spectra were computed from an analytical formula using the lag-1 autocorrelation of the EKE time series [Torrence and Compo, 1998, equation (16)]. The procedure is described by Belmadani *et al.* [2010] and allows deriving robust frequency spectra and identifying significant peaks.

Although there are some differences (which would be expected from the climatological simulation and from internal eddy variability), the ROMS and AVISO spectra are generally very similar (Figure A1). The annual time scale is seen in all the EKE spectra, although it is barely significant in the CTZ for AVISO. In the inter-annual band in the STF, there is energy at periods of 1.7–5 years in the two data sets. In the CTZ, the energy is slightly displaced toward lower frequencies in AVISO (2.5–5 years) compared to ROMS (1.7–5 years).

The downside of ensemble-averaging spectra over 5 year windows is that the spectral resolution is relatively low in the interannual band. We thus tested the sensitivity of these results by repeating the calculations for 10 year windows (three for AVISO, nine for ROMS). We again obtain similar results for ROMS and AVISO (Figure A2). The annual peaks are significant everywhere. In the CTZ, both data sets have energy at 3.3, 5,

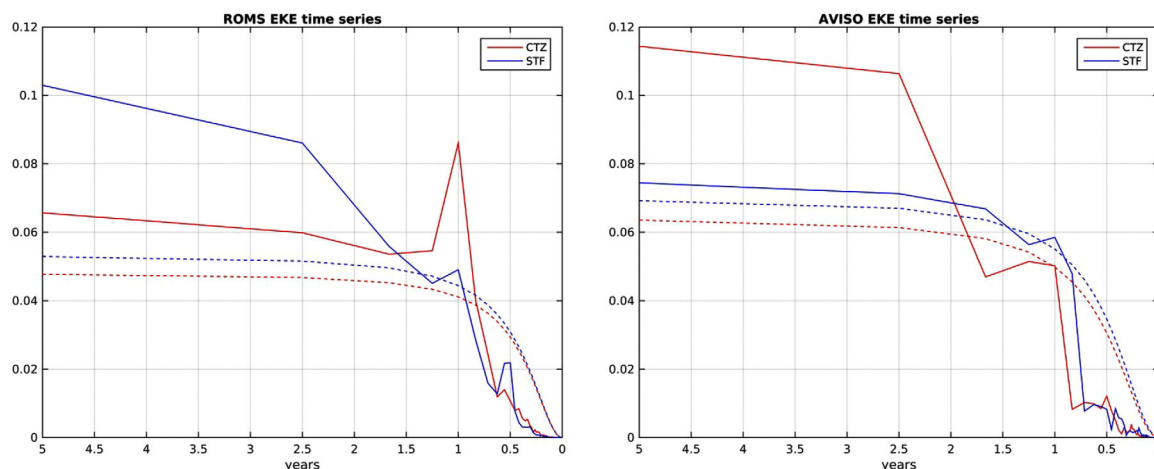


Figure A1. Normalized frequency spectra of the EKE time series shown in Figures 2b and 2d: ROMS (left) and AVISO (right). Dashed lines are for the red noise spectra. All the spectra were first computed over individual 5 year windows with 50% overlap and then ensemble-averaged.

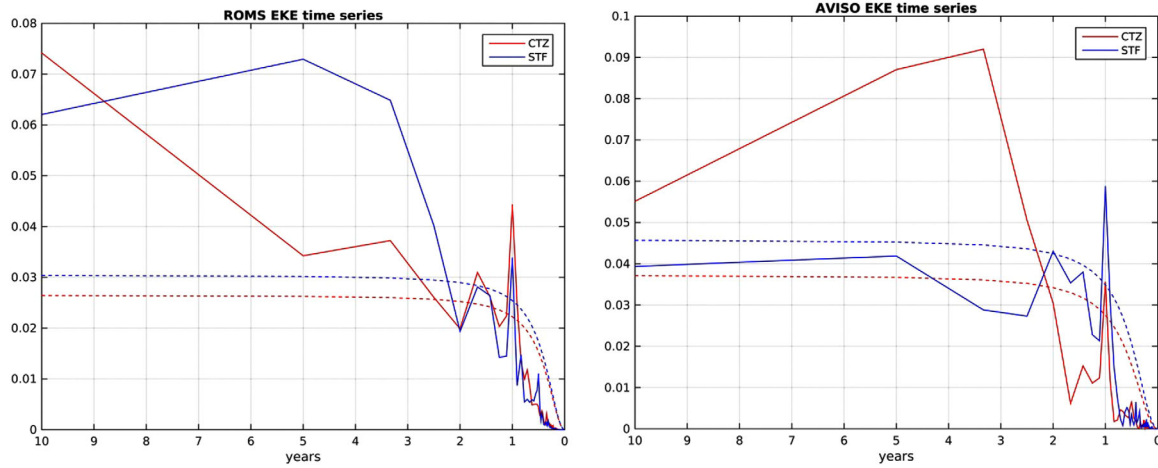


Figure A2. Same as Figure A1, except the individual spectra were computed over 10 year windows.

and 10 years (although their relative importance differ), while ROMS has an additional peak at 1.7 years. In the STF, AVISO does not have any significant peaks in the interannual band (except for a barely significant 2 year peak), while ROMS features energy at 3.3, 5, and 10 years. These peaks are present in AVISO too, but

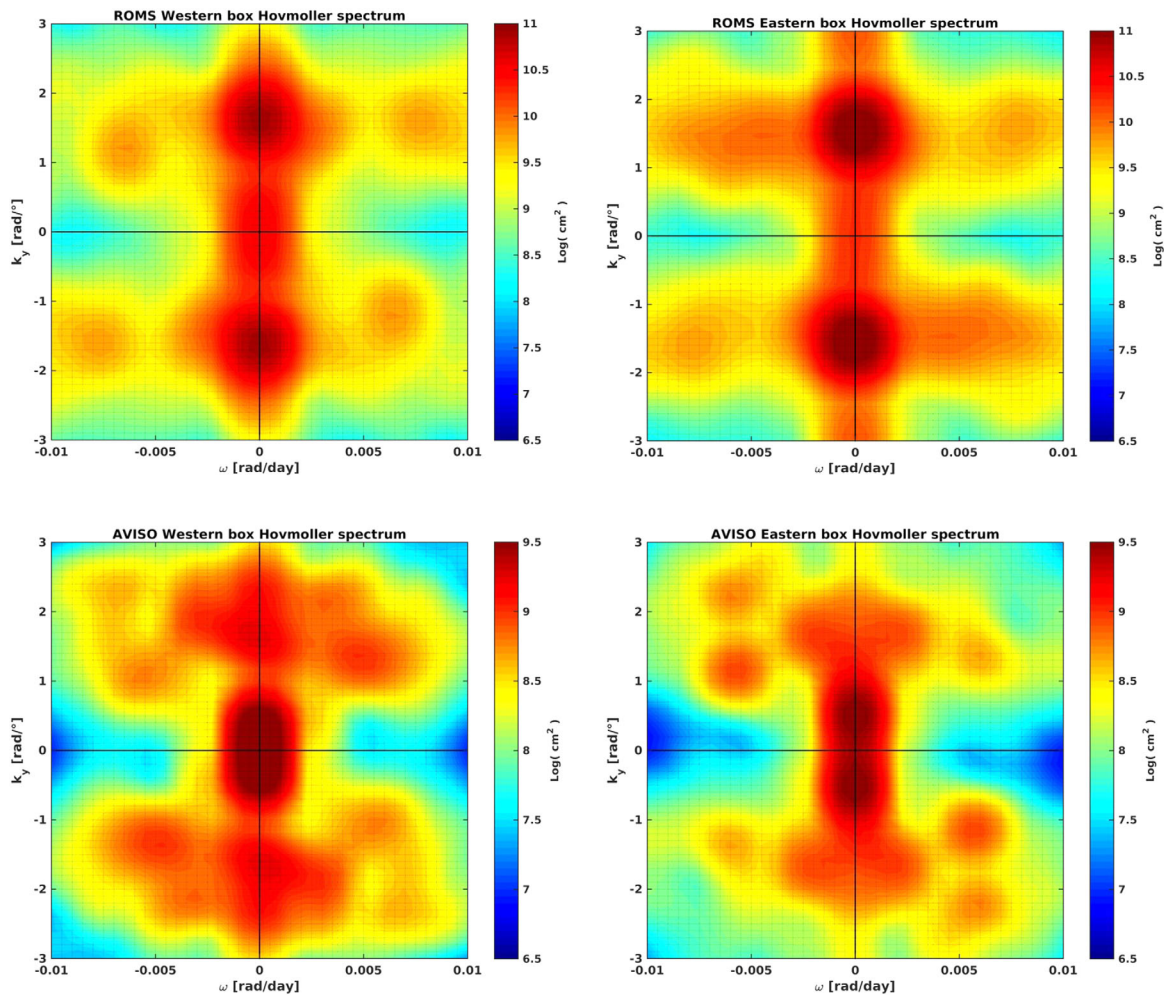


Figure A3. Frequency-meridional wave number power spectra of the Hovmöller diagrams shown in Figure 4: ROMS (top) and AVISO (bottom) in the western (left) and eastern (right) boxes. Note the logarithmic scale for spectral density, used to highlight secondary peaks.

they are not significant. Recall that only three spectra were ensemble-averaged for AVISO and that similar but significant peaks were found when using the 5 year windows. Overall, the FFT analysis confirms the similar temporal scales of model and observed eddy activity as inferred from the visual inspection of EKE time series (section 3.1).

To objectively analyze the stationary versus transient nature of striations in the model and altimetry data, 2-D Fourier analysis in the frequency-meridional wave number space (ω, k_y) was applied to the Hovmoller diagrams in Figure 5. The analysis allows extracting spatiotemporal scales for ROMS and AVISO in the western and eastern blocks, as well as meridional propagation speeds (similarly to the tilt for the k_x, k_y spectra).

There are a few differences between the two data sets (Figure A3): in particular, there is more energy on the larger meridional scales in AVISO ($k_y < 1$), which is likely a spurious effect due to quasi-zonal averaging, since these large scales are absent from the (k_x, k_y) spectrum (Figure 4b). AVISO spectra also have a larger number of secondary peaks, which results from the noisier Hovmoller plots (Figure 5).

On the other hand, there are a number of similarities between ROMS and AVISO in both regions: (i) most energy is concentrated in the mesoscale band ($L_y \sim 3-5^\circ$); (ii) maximum energy in this band is for stationary striations ($\omega = 0$), except perhaps for AVISO in the eastern box where there is a slight preference for southward (poleward) propagation; (iii) secondary peaks in the mesoscale band corresponding to both equatorward and poleward propagation can be found in all the figures at speeds of 100–200 km/yr; (iv) peaks corresponding to both propagation directions are of the same order in the western box (i.e., there is no clear propagation direction in either ROMS or AVISO); (v) there is a slight preference for poleward propagation direction (secondary peaks) in the eastern box for both data sets. Overall, ROMS reproduces spatiotemporal scales from AVISO in both regions reasonably well.

Acknowledgments

We are grateful to Pierre-Amaël Auger, William Kessler, Oleg Melnichenko, Bo Qiu, and Fabian Schloesser for stimulating discussions, to Vincent Combes and Vincent Echevin for their help in resolving some modeling issues, to Evan Mason for making the py-eddy-tracker code publicly available, and to two anonymous reviewers whose comments helped to greatly improve the quality of the original manuscript. The global database of tracked eddies was developed by Dudley Chelton and Michael Schlax and is available at <http://cioss.coas.oregonstate.edu/eddies/>. The SSALTO/DUACS altimeter SLA products were produced and distributed by the Copernicus Marine and Environment Monitoring Service (CMEMS) (<http://www.marine.copernicus.eu>). The altimeter ADT products were produced by SSALTO/DUACS and distributed by AVISO, with support from CNES (<http://www.aviso.altimetry.fr/duacs/>). MDT_CNES-CLS13 was produced by CLS Space Oceanography Division and distributed by AVISO, with support from CNES (<http://www.aviso.altimetry.fr/>). The CARS climatology is from the CSIRO Marine Laboratories. The SCOW scatterometer wind stress data can be downloaded at <http://cioss.coas.oregonstate.edu/scow/>. The ROMS simulations were performed on a PC cluster at DGEO/UdeC supported by Fondecyt Iniciación project 11130499, "Dynamics of Striations and Eddies off Central Chile." The OFES simulations were conducted on the Earth Simulator of the Japan Agency for Marine-Earth Science and Technology (JAMSTEC), and the outputs were accessed via the APDRC. E. Concha and D. Donoso were supported by Fondecyt Iniciación project 11130499. N. Maximenko was funded by NASA through grant NNX13AK35G. A. Chaigneau also acknowledges funding from the joint CNES/NASA OSTST project "Merging of satellite and in situ observations for the analysis of meso and submesoscale dynamics." IPRC/SOEST publication 1243/9981.

References

- Afanasyev, Y. D., S. O'Leary, P. B. Rhines, and E. Lindahl (2012), On the origin of jets in the ocean, *Geophys. Astrophys. Fluid Dyn.*, *106*(2), 113–137.
- Amante, C., and B. W. Eakins (2009), ETOPO1 1 arc-minute global relief model: Procedures, data sources, and analysis, *NOAA Tech. Mem. NESDIS NGDC-24*, 19 pp., U.S. Government Printing Office, Washington, D. C.
- Batteen, M. L. (1997), Wind-forced modeling studies of currents, meanders, and eddies in the California Current system, *J. Geophys. Res.*, *102*(C1), 985–1010.
- Beckmann, A., and D. B. Haidvogel (1993), Numerical simulation of flow around a tall isolated seamount, part I: Problem formulation and model accuracy, *J. Phys. Oceanogr.*, *23*, 1736–1753.
- Belmadani, A., B. Dewitte, and S.-I. An (2010), ENSO feedbacks and associated time scales of variability in a multimodel ensemble, *J. Clim.*, *23*(12), 3181–3204.
- Belmadani, A., V. Echevin, B. Dewitte, and F. Colas (2012), Equatorially-forced intraseasonal propagations along the Peru-Chile coast and their relation with the nearshore eddy activity in 1992–2000: A modelling study, *J. Geophys. Res.*, *117*, C04025, doi:10.1029/2011JC007848.
- Belmadani, A., N. A. Maximenko, J. P. McCreary, R. Furue, O. V. Melnichenko, N. Schneider, and E. Di Lorenzo (2013), Linear wind-forced beta-plumes with application to the Hawaiian Lee Countercurrent, *J. Phys. Oceanogr.*, *43*, 2071–2094, doi:10.1175/JPO-D-12-0194.1.
- Boé, J., A. Hall, F. Colas, J. C. McWilliams, X. Qu, J. Kurian, and S. B. Kapnick (2011), What shapes mesoscale wind anomalies in coastal upwelling zones?, *Clim. Dyn.*, *36*(11–12), 2037–2049, doi:10.1007/s00382-011-1058-5.
- Buckingham, C. E., and P. C. Cornillon (2013), The contribution of eddies to striations in absolute dynamic topography, *J. Geophys. Res. Oceans*, *118*, 448–461, doi:10.1029/2012JC008231.
- Buckingham, C. E., P. C. Cornillon, F. Schloesser, and K. M. Obenour (2014), Global observations of quasi-zonal bands in microwave sea surface temperature, *J. Geophys. Res. Oceans*, *119*, 4840–4866, doi:10.1002/2014JC010088.
- Cambon, G., K. Goubanova, P. Marchesiello, B. Dewitte, S. Illig, and V. Echevin (2013), Assessing the impact of downscaled atmospheric winds on a regional ocean model simulation of the Humboldt System, *Ocean Model.*, *65*, 11–24, doi:10.1016/j.ocemod.2013.01.007.
- Capet, X., F. Colas, P. Penven, P. Marchesiello, and J. C. McWilliams (2008), Eddies in eastern-boundary subtropical upwelling systems, in *Oceanic Modeling in an Eddy Regime*, *Geophys. Monogr. Ser.*, vol. 177, edited by M. W. Hecht and H. H. Hasumi, pp. 131–147, AGU, Washington, D. C., doi:10.1029/177GM10.
- Centurioni, L. R., J. C. Ohlmann, and P. P. Niiler (2008), Permanent meanders in the California Current System, *J. Phys. Oceanogr.*, *38*, 1690–1710, doi:10.1175/2008JPO3746.1.
- Chaigneau, A., and O. Pizarro (2005a), Eddy characteristics in the eastern South Pacific, *J. Geophys. Res.*, *110*, C06005, doi:10.1029/2004JC002815.
- Chaigneau, A., and O. Pizarro (2005b), Surface circulation and fronts of the South Pacific Ocean, east of 120°W, *Geophys. Res. Lett.*, *32*, L08605, doi:10.1029/2004GL022070.
- Chaigneau, A., A. Gizolme, and C. Grados (2008), Mesoscale eddies off Peru in altimeter records: Identification algorithms and eddy spatiotemporal patterns, *Prog. Oceanogr.*, *79*, 106–119, doi:10.1016/j.pocean.2008.10.013.
- Chaigneau, A., G. Eldin, and B. Dewitte (2009), Eddy activity in the four major upwelling systems from satellite altimetry (1992–2007), *Prog. Oceanogr.*, *83*, 117–123, doi:10.1016/j.pocean.2009.07.012.
- Chaigneau, A., M. Le Texier, G. Eldin, C. Grados, and O. Pizarro (2011), Vertical structure of mesoscale eddies in the eastern South Pacific Ocean: A composite analysis from altimetry and Argo profiling floats, *J. Geophys. Res.*, *116*, C11025, doi:10.1029/2011JC007134.
- Chelton, D. B., M. G. Schlax, and R. M. Samelson (2011a), Global observations of nonlinear mesoscale eddies, *Prog. Oceanogr.*, *91*, 167–216, doi:10.1016/j.pocean.2011.01.002.

- Chelton, D. B., P. Gaube, M. G. Schlax, J. J. Early, and R. M. Samelson (2011b), The influence of nonlinear mesoscale eddies on near-surface oceanic chlorophyll, *Science*, *334*, 328–332, doi:10.1126/science.1208897.
- Chen, R., and G. R. Flierl (2015), The contribution of striations to the eddy energy budget and mixing: Diagnostic frameworks and results in a quasigeostrophic barotropic system with mean flow, *J. Phys. Oceanogr.*, *45*, 2095–2113, doi:10.1175/JPO-D-14-0199.1.
- Chen, R., G. R. Flierl, and C. Wunsch (2015), Quantifying and interpreting striations in a subtropical gyre: A spectral perspective, *J. Phys. Oceanogr.*, *45*, 387–406, doi:10.1175/JPO-D-14-0038.1.
- Colas, F., J. C. McWilliams, X. Capet, and J. Kurian (2012), Heat balance and eddies in the Peru-Chile current system, *Clim. Dyn.*, *39*(1–2), 509–529, doi:10.1007/s00382-011-1170-6.
- Combes, V., S. Hormazabal, and E. Di Lorenzo (2015), Interannual variability of the subsurface eddy field in the Southeast Pacific, *J. Geophys. Res. Oceans*, *120*, 4907–4924, doi:10.1002/2014JC010265.
- Correa-Ramirez, M. A., S. Hormazabal, and G. Yuras (2007), Mesoscale eddies and high chlorophyll concentrations off central Chile (29°S–39°S), *Geophys. Res. Lett.*, *34*, L12604, doi:10.1029/2007GL029541.
- Cravatte, S., W. S. Kessler, and F. Marin (2012), Intermediate zonal jets in the tropical Pacific Ocean observed by Argo floats, *J. Phys. Oceanogr.*, *42*, 1475–1485, doi:10.1175/JPO-D-11-0206.1.
- Cushman-Roisin, B., and J. M. Beckers (2011), *Introduction to Geophysical fluid Dynamics: Physical and Numerical Aspects*, Int. Geophys. Ser., vol. 101, edited by R. Dmowska, D. Hartmann, and H. T. Rossby, 828 pp., Academic, Waltham, Mass.
- Davis, A., and E. Di Lorenzo (2015), Interannual forcing mechanisms of California Current transports II: Mesoscale eddies, *Deep Sea Res., Part II*, *112*, 31–41, doi:10.1016/j.dsr2.2014.02.004.
- Davis, A., E. Di Lorenzo, H. Luo, A. Belmadani, N. Maximenko, O. Melnichenko, and N. Schneider (2014), Mechanisms for the emergence of ocean striations in the North Pacific, *Geophys. Res. Lett.*, *41*, 948–953, doi:10.1002/2013GL057956.
- Ducet, N., and P.-Y. Le Traon (2001), A comparison of surface eddy kinetic energy and Reynolds stresses in the Gulf Stream and the Kuroshio Current systems from merged TOPEX/Poseidon and ERS-1/2 altimetric data, *J. Geophys. Res.*, *106*, 16,603–16,622.
- Dunn, J. R., and K. R. Ridgway (2002), Mapping ocean properties in regions of complex topography, *Deep Sea Res., Part I*, *49*(3), 591–604, doi:10.1016/S0967-0637(01)00069-3.
- Fu, L.-L., and R. Ferrari (2008), Observing oceanic submesoscale processes from space, *Eos Trans. AGU*, *89*(48), 488.
- Galperin, B., H. Nakano, H.-P. Huang, and S. Sukoriansky (2004), The ubiquitous zonal jets in the atmospheres of giant planets and Earth's oceans, *Geophys. Res. Lett.*, *31*, L13303, doi:10.1029/2004GL019691.
- Gill, A. E. (1982), *Atmosphere-Ocean Dynamics*, Int. Geophys. Ser., 30, edited by W. L. Donn, Academic, San Diego, Calif.
- Greatbatch, R. J., X. Zhai, J.-D. Kohlmann, and L. Czeschel (2010), Ocean eddy momentum fluxes at the latitudes of the Gulf Stream and the Kuroshio extensions as revealed by satellite data, *Ocean Dyn.*, *60*, 617–628, doi:10.1007/s10236-010-0282-6.
- Halo, I., B. Backeberg, P. Penven, I. Anson, C. Reason, and J. E. Ullgren (2014), Eddy properties in the Mozambique channel: A comparison between observations and two numerical ocean circulation models, *Deep Sea Res., Part II*, *100*, 38–53, doi:10.1016/j.dsr2.2013.10.015.
- Hormazabal, S., G. Shaffer, and O. Leth (2004), Coastal transition zone off Chile, *J. Geophys. Res.*, *109*, C01021, doi:10.1029/2003JC001956.
- Isern-Fontanet, J., E. García-Ladona, and J. Font (2003), Identification of marine eddies from altimetric maps, *J. Atmos. Oceanic Technol.*, *20*, 772–778.
- Ivanov, L. M., C. A. Collins, and T. M. Margolina (2009), System of quasi-zonal jets off California revealed from satellite altimetry, *Geophys. Res. Lett.*, *36*, L03609, doi:10.1029/2008GL036327.
- Ivanov, L. M., C. A. Collins, and T. M. Margolina (2012), Detection of oceanic quasi-zonal jets from altimetry observations, *J. Atmos. Oceanic Technol.*, *29*, 1111–1126, doi:10.1175/JTECH-D-11-00130.1.
- Kalnay, E., et al. (1996), The NCEP/NCAR 40-year reanalysis project, *Bull. Am. Meteorol. Soc.*, *77*, 437–471.
- Le Traon, P. Y., F. Nadal, and N. Ducet (1998), An improved mapping method of multi-satellite altimeter data, *J. Atmos. Oceanic Technol.*, *15*, 522–534, doi:10.1175/1520-0426(1998)015<0522:AIMMOM>2.0.CO;2.
- Maes, C., B. Blanke, and E. Martinez (2016), Origin and fate of surface drift in the oceanic convergence zones of the eastern Pacific, *Geophys. Res. Lett.*, *43*, 3398–3405, doi:10.1002/2016GL068217.
- Marchesiello, P., J. C. McWilliams, and A. Shchepetkin (2003), Equilibrium structure and dynamics of the California Current system, *J. Phys. Oceanogr.*, *33*, 753–783.
- Mason, E., A. Pascual, and J. C. McWilliams (2014), A new sea surface height-based code for oceanic mesoscale eddy tracking, *J. Atmos. Oceanic Technol.*, *31*, 1181–1188.
- Masumoto, Y., et al. (2004), A fifty-year eddy-resolving simulation of the world ocean—Preliminary outcomes of OFES (OGCM for the Earth Simulator), *J. Earth Simul.*, *1*, 35–56.
- Maximenko, N. A., B. Bang, and H. Sasaki (2005), Observational evidence of alternating zonal jets in the world ocean, *Geophys. Res. Lett.*, *32*, L12607, doi:10.1029/2005GL022728.
- Maximenko, N. A., O. V. Melnichenko, P. P. Niiler, and H. Sasaki (2008), Stationary mesoscale jet-like features in the ocean, *Geophys. Res. Lett.*, *35*, L08603, doi:10.1029/2008GL033267.
- Maximenko, N. A., P. Niiler, M.-H. Rio, O. Melnichenko, L. Centurioni, D. Chambers, V. Zlotnicki, and B. Galperin (2009), Mean dynamic topography of the ocean derived from satellite and drifting buoy data using three different techniques, *J. Atmos. Oceanic Technol.*, *26*(9), 1910–1919.
- Maximenko, N. A., P. Knudsen, L. Centurioni, O. Andersen, J. Hafner, and O. Melnichenko (2014), New mean dynamic ocean topography derived from a synthesis of satellite altimeter, gravity, and scatterometer data and trajectories of Lagrangian drifters, paper presented at 2014 Ocean Surface Topography Science Team Meeting, NASA, CNES, NOAA and EUMETSAT, Konstanz, Germany. [Available at http://meetings.avisio.altimetry.fr/fileadmin/user_upload/tx_ausyclseminar/files/30Red0900-1_OSTST_2014_Maximenko_et_al_edit.pdf]
- Melnichenko, O. V., N. A. Maximenko, N. Schneider, and H. Sasaki (2010), Quasi-stationary striations in basin-scale oceanic circulation: Vorticity balance from observations and eddy-resolving model, *Ocean Dyn.*, *60*, 653–666, doi:10.1007/s10236-009-0260-z.
- Morrow, R., F. Birol, D. Griffin, and J. Sudre (2004), Divergent pathways of cyclonic and anti-cyclonic ocean eddies, *Geophys. Res. Lett.*, *31*, L24311, doi:10.1029/2004GL020974.
- Nakano, H., and H. Hasumi (2005), A series of zonal jets embedded in the broad zonal flows in the Pacific obtained in eddy-permitting ocean general circulation models, *J. Phys. Oceanogr.*, *35*, 474–488.
- Pegliasco, C., A. Chaigneau, and R. Morrow (2015), Main eddy vertical structures observed in the four major Eastern Boundary Upwelling Systems, *J. Geophys. Res. Oceans*, *120*, 6008–6033, doi:10.1002/2015JC010950.
- Pujol, M.-I., Y. Faugère, G. Taburet, S. Dupuy, C. Pelloquin, M. Ablain, and N. Picot (2016), DUACS DT2014: The new multi-mission altimeter dataset reprocessed over 20 years, *Ocean Sci.*, *12*, 1067–1090, doi:10.5194/os-2015-110.
- Qiu, B., R. B. Scott, and S. Chen (2008), Length scales of eddy generation and nonlinear evolution of the seasonally modulated South Pacific Subtropical Countercurrent, *J. Phys. Oceanogr.*, *38*, 1515–1528, doi:10.1175/2007JPO3856.1.

- Rhines, P. B. (1975), Waves and turbulence on a beta-plane, *J. Fluid Mech.*, *69*, 417–443.
- Rhines, P. B. (1994), Jets, *Chaos*, *4*, 313–339.
- Richards, K. J., N. A. Maximenko, F. O. Bryan, and H. Sasaki (2006), Zonal jets in the Pacific Ocean, *Geophys. Res. Lett.*, *33*, L03605, doi:10.1029/2005GL024645.
- Rio, M.-H., S. Mulet, E. Greiner, N. Picot, and A. Pascual (2013), New global mean dynamic topography from a GOCE geoid model, altimeter measurements and oceanographic in-situ data, paper presented at 2013 Ocean Surface Topography Science Team Meeting, NASA, CNES, NOAA and EUMETSAT, Boulder, Colo. [Available at http://www.avisio.altimetry.fr/fileadmin/documents/OSTST/2013/oral/mulet_MDT_CNES_CLS13.pdf]
- Risien, C. M., and D. B. Chelton (2008), A global climatology of surface wind and wind stress fields from eight years of QuikSCAT scatterometer data, *J. Phys. Oceanogr.*, *38*, 2379–2413, doi:10.1175/2008JPO3881.1.
- Schlax, M. G., and D. B. Chelton (2008), The influence of mesoscale eddies on the detection of quasi-zonal jets in the ocean, *Geophys. Res. Lett.*, *35*, L24602, doi:10.1029/2008GL035998.
- Scott, R. B., B. K. Arbic, C. L. Holland, A. Sen, and B. Qiu (2008), Zonal versus meridional velocity variance in satellite observations and realistic and idealized ocean circulation models, *Ocean Model.*, *23*, 102–112, doi:10.1016/j.ocemod.2008.04.009.
- Shchepetkin, A. F., and J. C. McWilliams (2005), The regional oceanic modeling system: A split-explicit, free-surface, topography-following-coordinate ocean model, *Ocean Model.*, *9*, 347–404.
- Smith, T. M., and R. W. Reynolds (1998), A high-resolution global sea surface temperature climatology for the 1961–90 base period, *J. Clim.*, *11*, 3320–3323, doi:10.1175/1520-0442(1998)011%3C3320:AHRGSS%3E2.0.CO;2.
- Stramma, L., R. G. Peterson, and M. Tomczak (1995), The South Pacific Current, *J. Phys. Oceanogr.*, *25*, 77–91.
- Strub, P. T., J. M. Mesias, V. Montecino, J. Rutllant, and S. Salinas (1998), Coastal ocean circulation off western South America, in *The Sea*, vol. 11, edited by A. R. Robinson and K. H. Brink, pp. 273–314, John Wiley, New York.
- Taguchi, B., R. Furue, N. Komori, A. Kuwano-Yoshida, M. Nonaka, H. Sasaki, and W. Ohfuchi (2012), Deep oceanic zonal jets constrained by fine-scale wind stress curls in the South Pacific Ocean: A high-resolution coupled GCM study, *Geophys. Res. Lett.*, *39*, L08602, doi:10.1029/2012GL051248.
- Torrence, C., and G. P. Compo (1998), A practical guide to wavelet analysis, *Bull. Am. Meteorol. Soc.*, *79*, 61–78.
- van Sebille, E., I. Kamenkovich, and J. K. Willis (2011), Quasi-zonal jets in 3-D Argo data of the northeast Atlantic, *Geophys. Res. Lett.*, *38*, L02606, doi:10.1029/2010GL046267.
- Wang, J., M. A. Spall, G. R. Flierl, and P. Malanotte-Rizzoli (2012), A new mechanism for the generation of quasi-zonal jets in the ocean, *Geophys. Res. Lett.*, *39*, L10601, doi:10.1029/2012GL051861.
- Wang, J., M. A. Spall, G. R. Flierl, and P. Malanotte-Rizzoli (2013), Nonlinear radiating instability of a barotropic eastern boundary current, *J. Phys. Oceanogr.*, *43*, 1439–1452, doi:10.1175/JPO-D-12-0174.1.
- Yoshida, S., B. Qiu, and P. Hacker (2010), Wind-generated eddy characteristics in the lee of the island of Hawaii, *J. Geophys. Res.*, *115*, C03019, doi:10.1029/2009JC005417.
- Yoshida, S., B. Qiu, and P. Hacker (2011), Low-frequency eddy modulations in the Hawaiian Lee Countercurrent: Observations and connection to the Pacific Decadal Oscillation, *J. Geophys. Res.*, *116*, C12009, doi:10.1029/2011JC007286.